SLAC-J-ICFA-15
SLAC-PUB-7718
December 1997

HOME PAGE

http://www.slac.stanford.edu/pubs/icfa/

ICFA INSTRUMENTATION BULLETIN*

The publication of the ICFA Instrumentation Bulletin is an activity of the Panel on Future Innovation and Development of ICFA (International Committee for Future Accelerators).

Volume 15

• Fall 1997 Issue

* Supported by the Department of Energy, contract DE-AC03-76SF00515.

ICFA INSTRUMENTATION BULLETIN

The publication of the ICFA Instrumentation Bulletin is an activity of the Panel on Future Innovation and Development of ICFA (International Committee for Future Accelerators). The Bulletin reports on research and progress in the field of instrumentation with emphasis on application in the field of high-energy physics. It encourages issues of generic instrumentation.

Publisher : Stanford Linear Accelerator Center
SLAC Publications Department
Stanford, CA 94309, U.S.A.

Editor : J. Va'vra

Web Technical Advisers : J. Schwiening and T. Pavel

Cover: The illustration depicts L. J. Waghenaer's marine atlas, "The Mariner's Mirror," published in 1588. Lucas Janszoon Waghenaer was born in Holland in the 1530s. He became a famous ship pilot in his time. In 1584, he published the atlas ("Spieghel der Zeevaerdt") which was greatly valued among mariners for centuries. This was not due only to the map content, but also to the detailed knowledge of navigation techniques of that time. The atlas, as it appears on our page, is the same one used for the Dutch to English translation.

1997-98 Conference List

- 4-10 Jan 1998 , Aspen, CO
  ASPEN Winter Conference on Gravitational Waves and their Detection, Advanced Interferometer Topologies, Advanced Concepts in Suspensions and Noise.
  Aspen Center for Physics, 700 W. Gillespie Street: Aspen, CO 81611.

- Vienna Wire Chamber Conference '98
  23-27 February 1998, A-1050 Vienna, Nikolsdorfer Gasse 18, Austria.

Table of Contents

Streamers in MSGC's and other gaseous detectors

P. Fonte[1], V. Peskov[2,3], B.D. Ramsey[2]

1 LIP/Coimbra University and ISEC, Portugal,
2 NASA Marshall Space Flight Center,
3 National Research Council.

ABSTRACT

In this paper we describe the formation and propagation of streamers under different conditions and in different gas mixtures. We discuss how streamers may limit the operational capabilities of various gaseous detectors.

1. Introduction

Wire chambers, proposed by G. Charpak *et al.* [1], revolutionized detector development. They are widely used now in many experiments and have made possible many important discoveries in High Energy Physics. A further significant step was made by A. Oed et al. [2], who suggested replacing the wires by strips on a dielectric substrate.

This detector, the MSGC, has many technological advantages. However, it suffers from one main disadvantage: at gains of about 10^4 sparking appears and this is a serious limitation in many applications. Recent studies have shown that the gain is limited by the appearance of streamers [3] and that these streamers have a very narrow self-quenched region (in voltage) and then transit rapidly to sparks.

Do streamers affect the rate characteristics of MSGC's and other gaseous detectors and can breakdown in MSGC's be prevented? In this paper we will try to answer these questions.

2. What is known about streamers

2.1 PPAC

Historically, the first observations and systematic studies of streamers were done in Parallel-Plate Avalanche Chambers (PPAC's) [4] and we will summarize here the main conclusions.

At high gains in gaseous detectors two changes occur in the avalanche dynamics:

1) photons start to contribute to the avalanche development and cause a spread of the avalanches.
2) the space charge in the avalanche becomes sufficient to disturb the external electric field.

As a result, photoelectrons created outside the avalanche start to move towards it - Fig. 1. This may cause a growth of the avalanche in all directions and finally a streamer (a thin plasma filament) is formed. This occurs at some total charge in the avalanche (usually 10^8 electrons) corresponding roughly to the charge density at which the space-charge field becomes comparable to the applied field. This value seems to be an universal one in parallel-plate geometry at pressures close to or larger than 1 atm and is known as the Raether limit [4,5].

In any given gas mixture and pressure, streamers seem to propagate only in regions with applied fields larger than some critical value.

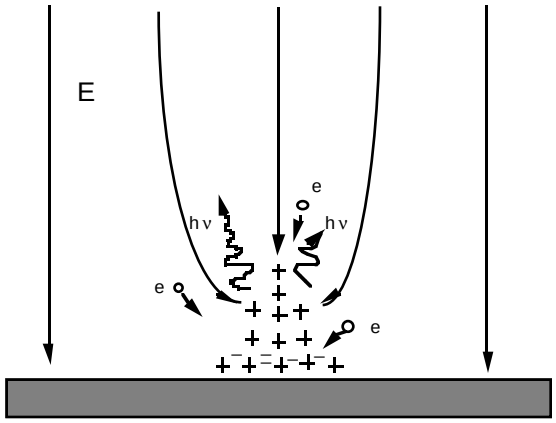

Figure 1 - Schematic drawing of streamer development.

Experimental studies [6] show that a streamer in its final stage has a structure very similar to a glow discharge. Note that in glow discharges an essential mechanism for sustaining the plasma is electron emission from the cathode spot and multi-step ionization in a positive column, i.e. ionization from excited states of atoms and molecules by electron impacts. Some authors [7] suggested that multi-step ionization also plays an important role in streamer formation. This helps to explain the propagation of streamers in gases with high concentrations of quencher when the photon mean free path is too small for photoelectrons to get sufficient multiplication.

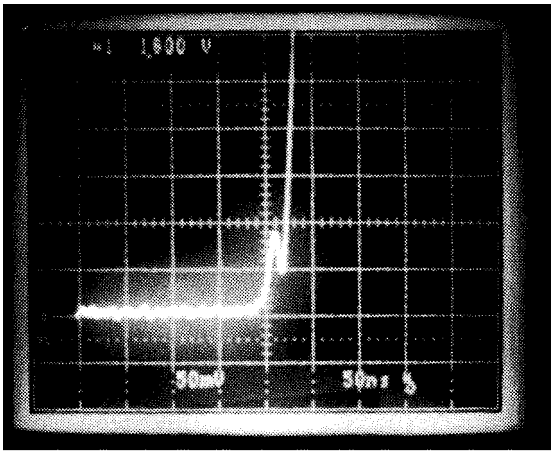

Figure 2 - Typical current pulse during breakdown in a PPAC [5].

When streamers reach the opposite electrode they may cause a powerful spark. In this case one observes precursors corresponding to the primary avalanche and then, with some delay, a current pulse corresponding to the propagation of the streamer and finally to the spark (see Fig. 2).

Many authors attempted to calculate the dynamics of avalanche to spark transition. Although models of streamer formation and development seem to reproduce well the experimental data [8], there is no comprehensive theory describing a streamer's transition to a spark when it touches the electrode [9]. It may be strongly dependent on electrode conductivity and surface conditions.

The main advantage of the PPAC is the ability to reach high gains (as was mentioned above the total charge in the avalanche before breakdown appears is usually about 10^8), and high rate capabilities ($>10^5$ counts/mm^2 sec). However, this total charge in the avalanche before breakdown is achievable only at rather low rates. At higher rates, the breakdown gain is usually inversely proportional to the counting rate. One possible reason for this is that avalanches overlapping in time and space effectively add their respective ion charges [5].

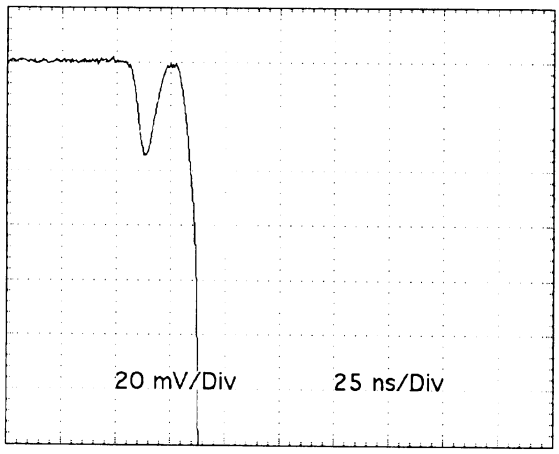

Figure 3 - Current pulse at breakdown in a RPC [11].

2.2 Streamer chambers

Streamer development in PPAC's can be restricted if a very short duration high-voltage pulsed is applied. This principle was realized in the so called "streamer chambers", which were actively used in many experiments [10]. The streamer chamber works in a "waiting" mode. A passing charged particle produces ionization inside the chamber and also generates a signal in a trigger system located outside the detector volume. This signal in turn triggers a short (~10 ns) high-voltage pulse, which initiates streamer development. Since the high-voltage pulse is very short, streamers are generated very close to the position of the initial ionization and do not produce any sparks. Such streamers emit enough light to be recorded optically which allows reconstruction of the track. If a longer duration high-voltage pulse is applied, streamers transit to sparks. This principle is realized in the so called “spark chambers” [4].

2.3 RPC

In Resistive Plate Chambers (RPC's) one or both electrodes are made from materials with high resistivity (usually > 10^{10} Ω cm).

In principle there should be no significant difference in streamer formation and their initial development between the PPAC and the RPC. Indeed, the same current pulse features were observed in both the RPC and the PPAC-see Figs. 2 and 3 [5,11,12]. However, the final streamer stages and especially the power dissipated in the sparks is different. Roughly speaking, the power dissipated in sparks depends on the effective discharge capacities. In the case of metallic electrodes a considerable part of the charge accumulated in the detector will be discharged through the spark.

In the case of the RPC local charging of the resistive electrode by the spark current renders the effective capacitance very low. As a consequence, sparks created by streamers in the RPC will be weak. This is why in many papers these weak sparks were called "streamers " although they are not actually real streamers.

Power dissipated in sparks also depends on the gas mixture. For example, in freon mixtures the electron charge released by a spark could be very small, about 1 pC [13].

For RPC’s the maximum achievable gain is also inversely proportional to the counting rate, but this dependence is much steeper than in the case of the PPAC. The primary reason for this dependence is not the appearance of breakdown due to avalanche overlapping, but simply charging of the dielectric electrodes of the RPC. The best rate characteristics, so far, were obtained with Pestov (electronic) glass electrodes [14]. Spatial resolutions achieved with such detectors were better than 0.1 mm. Note that when metallic readout strips were placed inside the gas gap between the electrodes the rate capability approached that of the PPAC [15].

2.4 Detectors with anode wires

2.4.a Single wire counter and multiwire chambers

As was described above, in uniform fields streamers are usually unquenched and once started continue to develop until they touch the opposite electrode.

It was found that streamers also can be formed in detectors with non-uniform fields, for example in single wire counters and multiwire chambers (MWPC) [16,17]. The main feature of these streamers is that they start to propagate perpendicularly to the anode wire, but usually they do not reach the cathode due to the fast field drop with distance from the anode (see Fig. 4). As a consequence they do not trigger sparks and are somehow "self quenched". Note that these streamers appear only in detectors with rather thick anode wires (>50 μm). In the case of thin wires, the field drops so fast with distance that at high gains discharges start to propagate along the wire (the so-called Geiger or limited-Geiger mode) [18].

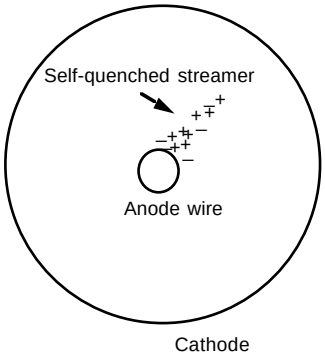

Figure 4 - Self-quenched streamer in detectors with thick anode wires.

How do these self-quenched streamers reveal themselves experimentally?

When streamers appear one can observe a jump in amplification, as shown in Fig. 5. The other typical characteristic of streamers is an intense (>10 μA) and short (<50 ns) current pulse. In some cases streamers can be recorded optically.

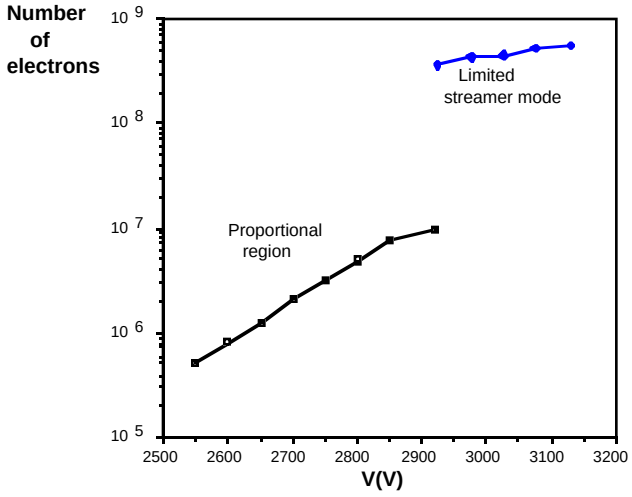

Figure 5 - Total charge in avalanche vs. voltage in wire detectors operating in proportional and streamer mode [17]

The gas gains at which streamers appear depend not only on the detector geometry, but on the gas mixture and pressure - see Figs. 6a and 6b. From this figure one can see that there is an optimum concentration of the quencher at which the gain reaches the highest values.

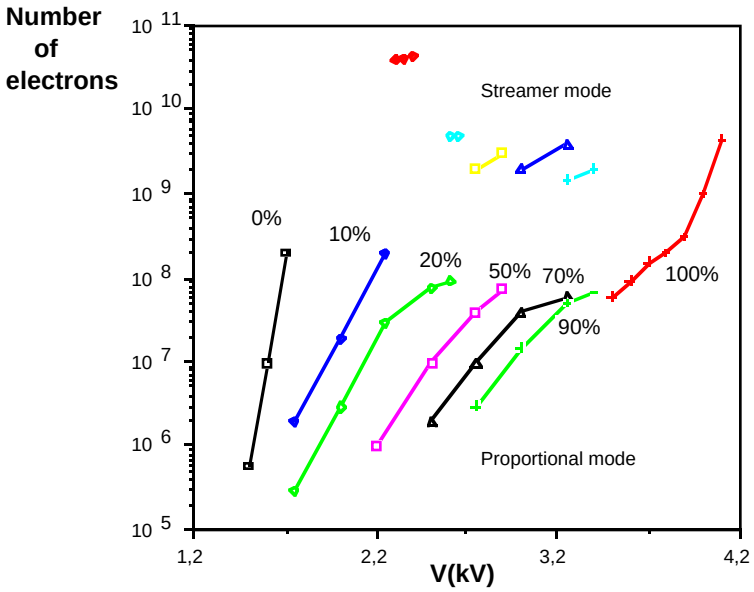

Figure 6 a - Total charge in avalanche at which streamers develop in a single wire counter for various methane concentrations in Ar/CH_4 mixtures [19]

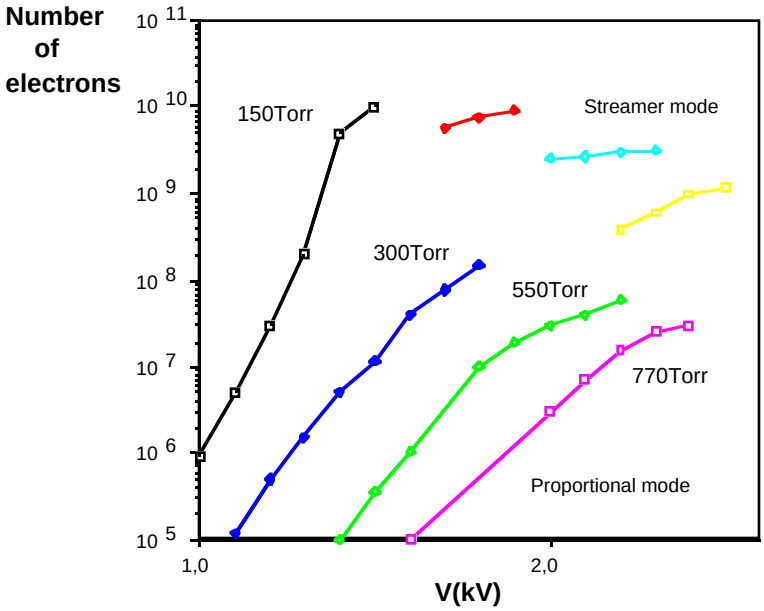

Figure 6 b - Total charge in avalanche at which streamers develop in a single wire counter for various total pressures in Ar + 25% iC_4H_{10}.

The maximum charge in avalanches at which streamers appear also depends on noble gas: it is maximum in He and Ne-based mixtures and minimum in Xe-based mixtures (see Fig.7)

In [19] it was claimed that in some pure quenching gases at 1 atm, CH_4 for example, no streamers develop at all (see Fig. 6a). The same is also true at low pressures (p<0.3 atm) for most of the mixtures tested in [19] (see Fig. 6b).

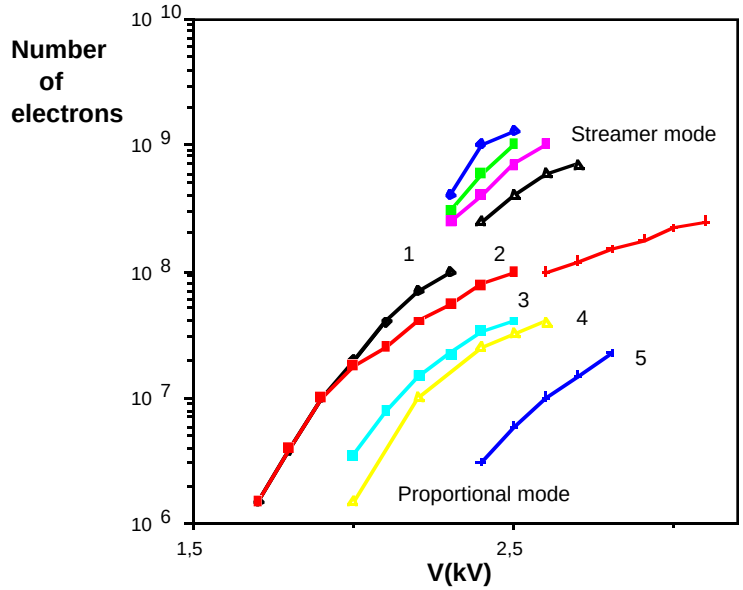

Figure 7 - Total charge in avalanche at which streamers appear in various noble gases [19].
1 - He + 25% iC_4H_{10} 2 - Ne + 25% iC_4H_{10}
3 - Ar + 25% iC_4H_{10} 4 - Kr + 25% iC_4H_{10}
5 - Xe + 25% iC_4H_{10}

2.4.b Streamers in asymmetric wire chambers

Asymmetric wire chambers are the next generation of detectors and were invented to improve the rate capability of the MWPC [20]. In fact, they have a geometry similar to the MSGC, but the strips are replaced by wires and there is no substrate. A short distance and strong field between anodes and cathodes allows fast removal of positive ions.

In asymmetric wire chambers streamers may also occur at total a charge in avalanche larger than about $2\text{-}5\times10^6$ electrons [3,21].

3. Streamers in gaseous detectors with substrate

3.1 Streamers in asymmetric wire chamber with substrates

What will happen when we place the wires of the asymmetric wire chamber in direct contact with a dielectric surface? In this case streamers also occur (at a total charge in avalanche slightly less than without substrate), but they are unquenched. So the presence of the surface changes the streamer's development.

Self-quenched streamers are only observed occasionally, at low gains. Note that wires should be in firm contact with the surface otherwise charging will occur and the gain will drop with time [22].

3.2 Streamers in uncoated MSGC's

It was discovered recently [3] that in the case of MSGC's the maximum achievable gain is also limited by streamers, as in asymmetric wire chambers with substrates. A typical waveform of the current pulse of a streamer in a MSGC is presented in Fig. 8. Usually the streamer current pulses are shorter than 50 ns and have amplitudes up to a few mV on 50 Ω.

In some gases, for example with TMAE vapor, the streamers were clearly observed visually in a dark room (note that in this case the gas chamber with MSGC and all gas system was heated to 40 Cº to increase the partial pressure of TMAE). As in the case of the asymmetric wire chamber with substrates, streamers in MSGC's have a very narrow (in voltage) self-quenched region and then transit rapidly to sparks. These sparks were very bright and could be seen easily even in an illuminated room.

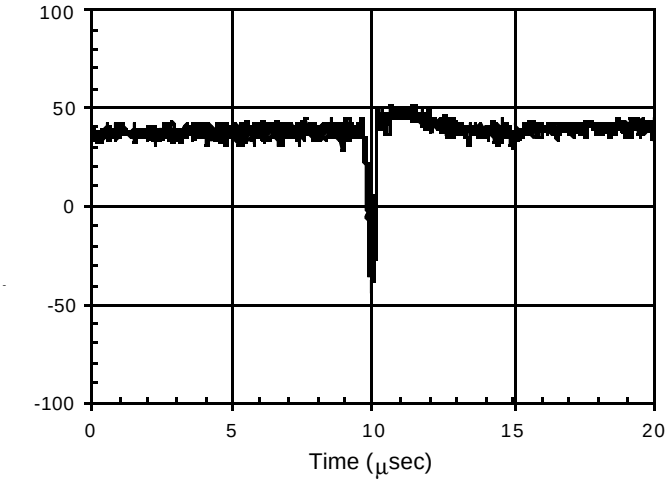

Figure 8 - Streamer current pulse in a MSGC (on 50 Ω).

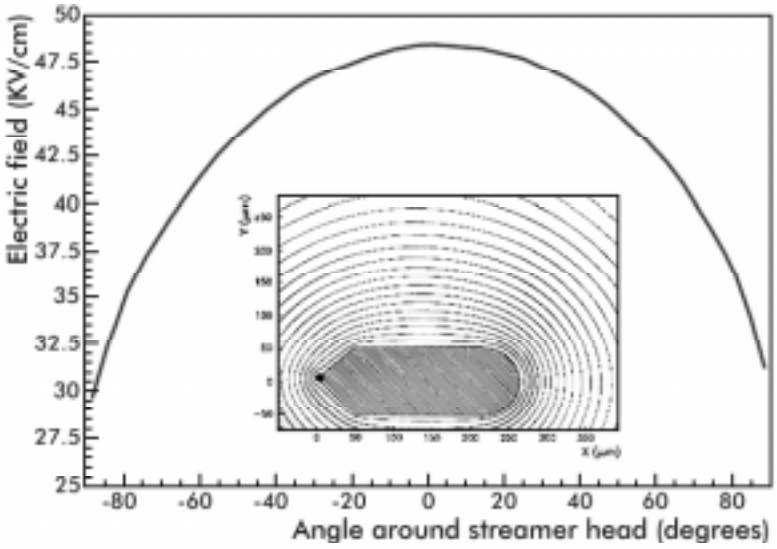

Figure 9 a - The field strength around the tip of a streamer. The inset details a map of equipotential lines for a streamer near an anode wire.

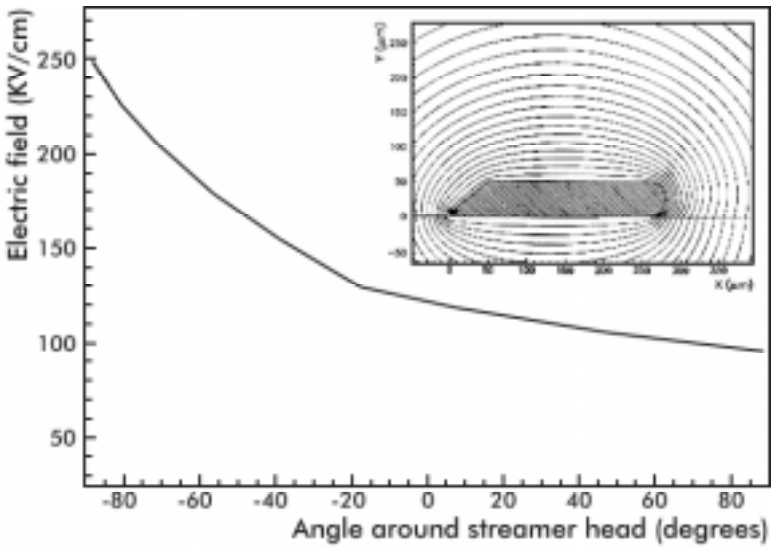

Figure 9 b - The same for a streamer in the presence of a surface.

Why are the streamers unquenched in the presence of a substrate?

This can be understood from calculations of the field near the streamer head. In these calculations the streamer was considered as a conductive medium (plasma actually), kept at the anode potential. Figs. 9a and 9b show calculations of the field near the streamer (diameter 100 μm, length 250 μm) for an asymmetric wire chamber without and with substrate. One can clearly see that when the substrate is present there is a high local electric field between the head of the streamer and the substrate, due to dielectric polarization. This is therefore the region of the most intense ionization during the streamer propagation. Thus, the streamer, when it is close to the dielectric surface, creates the high field necessary for its own propagation.

These streamers are very similar to the well known "gliding" discharges [23]. Gliding discharges are two dimensional and, due to the extreme "sharpness" of the edges of the surface space-charge layer, the transition from surface avalanche to the spark type of breakdown occurs at much lower electric fields than in the usual "three dimensional" case [23].

Calculations also show that points where the metal electrode structures touch the dielectric substrate have a very high electric field. These points are favorable for the initiation of avalanches close to the surface and the formation of surface streamers.

Are there any ways to limit streamer formation? This could be done by optimization of the MSGC and by developing substrate-free detector designs.

3.3 Optimization of uncoated MSGC's

As was described above, in the case of detectors with thin anode wires (< 20 μm) streamers cannot touch the cathode due to the fast drop of radial electric field. By analogy one can think that in order to suppress the streamers and therefore increase the maximum gain before breakdown in the MSGC, the multiplication region should be concentrated to a narrow region around the anode strips and that the gas gain elsewhere should be maximally suppressed.

Of course, the real situation is more complicated because streamers create their own field. Since the calculations of streamer dynamics is rather complicated the easiest way to check the validity of our assumption is experimentally. One can try to concentrate the multiplication near the anode strips in several ways: by reducing the anode width, by increasing the anode-cathode gap and by using mixtures having a sharp dependence of gain vs. voltage. A systematic experimental study performed recently fully confirms that optimizing these parameters allows higher gains to be

reached in MSGC's (see [24] for more details). As an example, Fig. 10 presents results obtained with different pitches and anode widths.

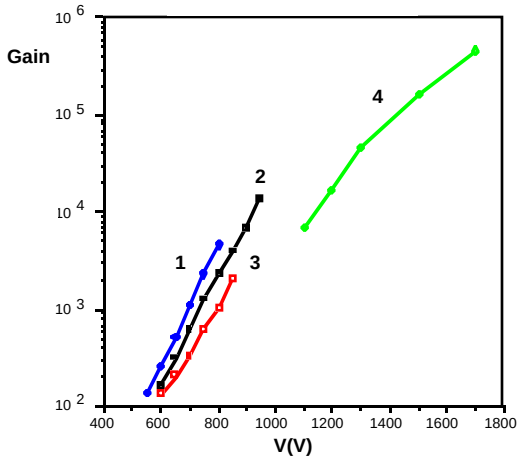

Figure 10 - Maximum achievable gains in MSGC's with different anode widths and pitches:

1 - 1 mm pitch, 10 μm anode width
2 - 2 mm pitch, 10 μm anode width
3 - 1 mm pitch, 25 μm anode width
4 - strips and wires on substrate at 2 mm pitch (see Fig.12).

One can clearly see that the highest gains were achieved with narrow anodes and at high pitches. In Fig. 11 are presented the gain vs. voltage curves for Ar/CH_4 mixtures and different concentrations of CH_4. One can see that the maximum achievable gain behaves similarly to what was observed in a single-wire counters (see Fig. 6). The highest gains in this particular mixture were achieved in pure CH_4. This result is in excellent agreement with those obtained for streamers in single-wire detectors - see Fig. 6.

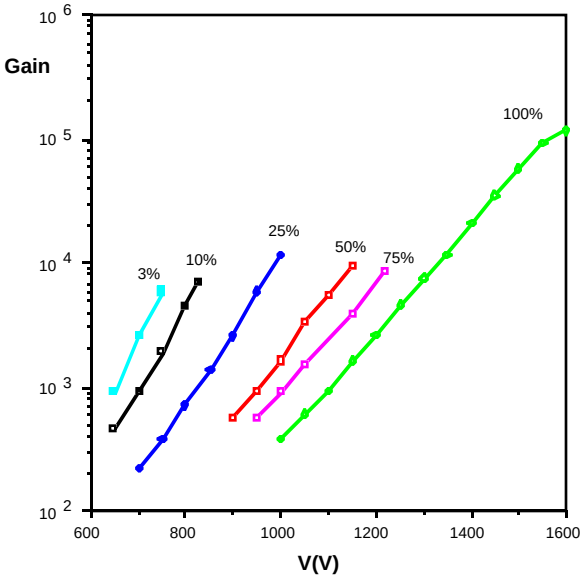

Figure 11 - Maximum achievable gain in an MSGC operating in Ar/CH_4 mixtures for various CH_4 concentrations

It was found also that the maximum achievable gain depends on the noble gas [25]. The highest gains were achieved in He and Ne-based mixtures and lowest in Xe-based mixtures. These results are in a good qualitative agreement with those obtained with single wire counters (see Fig. 7).

Despite the good qualitative agreement between streamer onset properties in MSGC's and single wire detectors the charge needed for streamer development is two orders of magnitude lower in the former case. This may be attributed to the two dimensional nature of the streamer discharge in MSGCs, which will be more concentrated than the three dimensional streamer formed in single wire detectors.

New geometries of microstrip detectors were also tested. In one of these, cathodes were made from thick wires of diameter 0.75 and 1 mm touching the surface or suspended just above it (see Fig. 12). In such designs, we tried to minimize the contribution of the substrate and reduce the field near the cathode. The gain achieved with such devices was 10^5 or higher (see Fig. 10 - curve 4). All these results confirm the assumption that the gain should be concentrated near the anodes.

As a result of this work on MSGC's optimization, the authors of ref. [26] were able to get a uniform gain of 10^4 over a MSGC of surface area 30×30 cm^2 with 2 mm pitch, 10 μm anodes strips and a Penning mixture (Xe+2% isobutylene at 2 atm) having a sharp dependence of gain vs. voltage. The probability of breakdown is proportional to the detector's surface area. However, not a single breakdown was observed over a week of continuous operation of the detector at this gain.

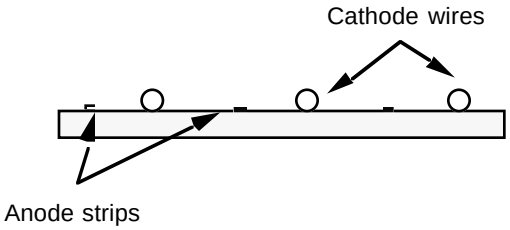

Figure 12 - Example of a MSGC design which permits the highest gains.

3.4 Streamers in coated MSGC's

At high counting rates the dielectric substrate of the MSGC's is charged by positive ions from avalanches causing gain variations with time. One solution to this problem is coating the substrate with a thin, higher conductivity layer (e.g. diamond). In MSGC's with conductive coated substrates the mean field along the surface between anodes and cathodes increases and, what is even more important, becomes more uniform [22]. This is favorable for streamer propagation and as a result the maximum achievable gain is lower compared to bare MSGC's.

Another feature of coated MSGC's is high amplitude spurious pulses which can also trigger breakdown. The nature of these pulses is discussed in [22,27].

3.5 Microgap Gas chambers

The Microgap Gas Chamber (MGC) was developed by F. Angelini *et al* . [28] in an attempt to solve the charging problem of MSGC. The main feature of this type of detector is a very short gap between anodes and cathodes allowing fast removal of ions produced by avalanches. As a result no charging effect was observed even at rates up to 10^7 counts/mm^2 sec. However the maximum achievable gain is also limited to 10^4.

Our recent results with MGC's [29] reveal many similarities with MSGC pre-discharge features. We concluded that breakdown in these detectors occurs through a streamer mechanism as in MSGC's. It is not surprising since part of the avalanche touches the dielectric surface and may form a surface streamer.

It is interesting to note that the maximum achievable gain in the MGC depends on the gas mixture in a way similar to high pitch MSGC's. There is also one optimum concentration of quencher at which the gain reaches a maximum, and the highest gains were achieved in He and Ne-based mixtures, the lowest in Xe-based mixtures [30].

4. New types of high-rate gaseous detectors.

The low achievable gains in ordinary MSGC's stimulated different groups to develop another designs of high-rate gaseous detectors. A relevant example could be the Microdot Gas Avalanche Chamber [31,32]. The main feature of this design is that the anodes are metalized dots on a substrate and the cathodes are coaxial rings. This geometry insures fast drop of electric field with distance from the anode dots and as a consequence allows higher gains ($> 10^4$) to be achieved [32]. However, even in this design streamers may develop at high gains as was clearly shown in [31].

Another example of a new high-rate detector could be the recent MICROMEGAS [33]. MICROMEGAS is just a PPAC with a small (~0.1 mm) gap between electrodes. There are at least two advantages of this design:

1) the small size of the gap and hence the avalanche reduces the effective area of the induced charge on the anode strips. Thus by using small pitch strips a better position resolution in principle could be achieved,
2) a small gap also guaranties a fast removal of positive ions and hence less space charge effect at high rates.

MICROMEGAS permits gains of 10^4-10^5 [34]. At higher gains breakdown appears, presumably through the streamer mechanism. However in a new design with narrow anode strips it was possible to explore additional multiplication in non-uniform field near the anode strips, permitting an additional factor of 5 or more in gain [34].

Other examples of new high rate gaseous detectors in which the role of substrate was minimized could be CAT [35] and GEM [36]. In these detectors amplifications occur in "holes" in substrate. There were no reports on breakdown studies in these devices, but since part of the avalanche touches the dielectric surface one can assume that it may occurs through the surface type of discharge.

5. Potential limitations of high-rate gaseous detectors

In general one can assume that in any high-rate detector, fast removal of ions requires a short distance between anodes and cathodes, as well as an high and uniform field. But these are also favorable conditions for streamer development. Additionally, at high counting rate, avalanches start overlapping in space and time [5] and this lowers the maximum achievable gain at which streamers appear. This effect is also proportional to the detector surface area, so streamers always appear soon or later just due to statistics. So, large-surface high-rate detectors are specially prone to suffer from streamers.

Another effect in some types of high-rate detectors is cathode "excitation". It was observed that under ion bombardment the work function of the cathode may be reduced [37] and additionally it may emit electrons [22, 38]. This emission may continue for several minutes. Due to these effects, after one breakdown another breakdown or a series of breakdowns may appear at the same place [38]. One can stop these continuous breakdowns by lowering the working voltage for a few minutes, which is obviously not a practical solution for a high-rate device.

It looks that all high rate gaseous detectors may suffer from streamers or continuous breakdown. As a result, for reliable operation one should lower the gain at high rates.

6. Conclusion

Experience shows that all detectors are rate limited for one or another reason. We described in this paper how streamers could play an important role.

In uniform fields, or when the attached to a dielectric surface, streamers are unquenched and once started continue to develop until they reach the cathodes. As follows from this paper, in substrate-free detectors and especially in geometries providing non-uniform fields one can reach the highest gains. An example could be recent modification of MICROMEGAS where amplification in non-uniform fields near anode strips was observed [34]

References

[1] G. Charpak et al., Nucl. Instr. and Meth. 62 (1968) 262

[2] A. Oed, Nucl. Instr. and Meth. A263 (1988) 351

[3] V. Peskov et al., "Surface streamer breakdown mechanisms in MSGC", to appear in Nucl. Instr and Meth.

[4] H. Raether, "Electron avalanches and breakdown in gases", Butterworths, Washington, 1964

[5] P. Fonte et al., Nucl. Instr. and Meth. A310 (1991) 128

[6] E. Marode, Journal of Applied Phys. 46, (1975) 2005,
E. Marode, Journal of Applied Phys. 46, (1975) 2016

[7] L. S. Zhang, Nucl. Instr. and Meth. 247 (1986) 343
V. Peskov, Sov. Phys. Tech. Phys. 20 (1976) 1584

[8] P. Fonte, IEEE Trans. Nucl. Science, vol. 43, 3 June 1996, pp. 2135.

[9] Yu. P. Raizer, "Gas discharge Physics" Springer-Verlag, 1991

[10] L. S. Schroeder, Nucl. Instr. and Meth. 162 (1979) 395

[11] D. F. Anderson et al., Nucl. Instr. and Meth. A348 (1994) 324

[12] I. R. Cardarelli, Nucl. Instr. and Meth. A382 (1996) 470

[13] A. D. Ciaccio et al., Proceedings of the 3d International Workshop on Resistive Plate Chambers and Related Detectors", Edd. S. P. Ratti, M. Merlo, INFN Pavia, Italy 1996, 263

[14] V. Peskov, " High rate RPC" report at the US/CMS Meeting at the Univ. of Wisconsin, Madison, 1994

[15] I. Crotti et al., "RPC with secondary electron emitters and microstrip readout" report at the IEEE Nucl. Science Symposium, Anaheim 1996

[16] G. Alekseev et al., Nucl. Instr. and Meth. 177 (1980) 385

[17] M. Atac et al., Nuclear Instr. and Meth. 200 (1982) 345

[18] E. Funfer, H. Neuert, "Radiation counters", Gosatomisdat,1961 (in russian)
G. D. Bogomolov et al., Prib. Techn. Exp, 21 (1978) 639

[19] A. Nohtomi, "Study on operation mechanism of gas counters in self-quenched streamer mode" Doctoral Thesis, Kyushu Univ. Fukuoka, Japan, 1995

[20] G. Charpak et al., Preprint CERN/AT/94-07 (ET),1994

[21] I. Giomataris, private communication

[22] V. Peskov et al., "Feedback and Breakdown in MSGC" accepted for publication in Nucl. Instr. and Meth.

[23] K. Uhlig, "Surface discharges in high magnetic fields", Hartung-Gorre Verlag, 1991

[24] B. D. Ramsey et al., "A study of factors limiting maximum gain in MSGC" to appear in IEEE Trans. Nucl. Science, 1997

[25] R. Bellazzini, private communication

[26] B. D. Ramsey et al., Nucl. Instr. and Meth. A383 (1996) 424

[27] V. Peskov et al., "Breakdown features of various MSGC designs and their improvements" submitted to IEEE-97 Symposium

[28] F. Angelini et al., Nucl. Instr. and Meth. A 335 (1993) 69.

[29] V. Peskov, B. Ramsey, "Energy resolution of MGC's at high pressure", unpublished data.

[30] J. Van der Marel, "Microstrip and Microgap Chambers", PhD. Thesis, Delft University, 1997.

[31] D. Mattern et al., Nucl. Instr. and Meth. A300 (1991) 275.

[32] S. F. Biagi, "Microdot Chambers" report at the Manchester Conf. on Position Sensitive Detectors, Manchester, UK, 1996

[33] I.Giomataris et al., Preprint DAPNIA/SED 95-04,1995

[34] I. Giomataris, Private communication

[35] F. Bartol et al., J. Phys III 6 (1996) 337

[36] F. Sauli, Nucl. Instr. and Meth. A386 (1997) 531

[37] G. F. Karabadjak et al., Nucl. Instr. and Meth. 217 (1983) 56

[38] Y. Ivaniouchenkov et al., "The high-rate behavior of Parallel Mesh Chambers", report submitted to the IEEE-97 Nuclear Science Symposium.

October 12, 1997

SOFT X-RAY PRODUCTION IN SPARK DISCHARGES IN HYDROGEN, NITROGEN, AIR, ARGON, AND XENON GASES

J. Va'vra
Stanford Linear Accelerator Center, Stanford University,
Stanford, CA 94309, U.S.A.

J. A. Maly
Applied Science Consultants
5819 Ettersberg Dr., San Jose, CA 95123, U.S.A.

P. M. Va'vra
67 Pine Lane, Los Altos, CA 94022, U.S.A.

ABSTRACT

We describe a generator of soft X-rays of energy between 2 and 10 keV by sparking in hydrogen, air, nitrogen, argon, and xenon gases at low pressure with a sparking voltage as low as ~0.8 kV, which can be used as a simple monitor of the gaseous detectors. The X-ray production mechanism is also discussed, including the possibility of a new process.

(Submitted to Nuclear Instruments and Methods)

1. INTRODUCTION

We present a simple X-ray generator which can be used to monitor drift chambers. The generator uses a spark gap operating at low pressure, with a thin window and very low voltages between 0.8 and 2.5 kV to create X-rays between 2 and 10 keV.

To create the X-rays by sparking in low pressure is not new. Less known is the fact that one can create the X-ray energies, which are larger than the sparking voltage. This seemingly surprising effect is semi-qualitatively explained in the literature by the so called "pinch" effect [1-4], which is known to occur during very large low inductance sparks, operating typically with initial charging voltages of 10-60kV, charging capacitance of 10-20μF, low inductance of ~100 nH, stored energies of 1-3 kJ/pulse, and peak spark currents of 100-200kA [1]. The pinch effect has been demonstrated experimentally using pin hole photography, which indicates a formation of point-like (plasma points) regions within the plasma [2]. A generally accepted explanation of the pinch effect is based on the radiation collapse model [1]. During the pinch effect, one observes a formation of dips in spark current, which in turn creates large local voltages [1]. The voltage across the sparking gap can exceed the supply voltage by a factor of 2-3 [3], and thus, the X-ray energies can exceed the sparking voltage. The current dips are correlated with the appearance of plasma points, which principally emit X-ray lines of the anode material; radiation from the cathode material is weak [1]. The X-ray production shows a strong angular anisotropy [4]. The sparks in the above tests are so

large that the electrodes wear out quickly. Indeed, the spectral investigations reveal emission from heavily ionized atoms, which are present in the electrode material [2].

In our tests, we tried to set the smallest possible sparks that are still consistent with the X-ray production, i.e., we tried to operate at the opposite end of the spark's stored energies, as mentioned above. The sparking voltage varied between 0.8 and 2.1kV, the charging capacitance was 75nF, inductance was ~1000nH, stored energy was 0.024-0.17J/pulse, the peak spark currents were 0.2-0.5kA, and the total spark charge was between $4x10^{14}$ and 10^{15} electrons/spark. The observed X-ray energies were between 2 and 10 keV, even at the lowest sparking voltage of ~0.8kV (depending on the gas), and followed an exponential distribution falling towards larger X-ray energies. The maximum observed X-ray energy (~10keV), generated at the lowest voltage (~0.8kV), is above K-shell energy of typical gases we used in our tests, and materials used in our spark electrodes (see Table 1 and Chapter 4). The X-ray production persists even for the carbon electrodes which have the smallest K-shell energy (0.284keV); this would appear to eliminate a theory that the electrode atoms are responsible for the X-ray production. Furthermore, we have evidence that the production threshold and the X-ray rate are dependent on the gas choice in the sparking vessel. We have measured the I(t), V(t), and dI/dt(t) curves and have confirmed that the X-rays are produced during the largest swing in the dI/dt(t) curve corresponding to a dip in the current I(t). This would appear to be consistent with the earlier mentioned pinch effect mechanism. The sparks in our tests are relatively large by a typical standard, however, compared to the spark energies used in Refs.1-4, they are considerably smaller, by at least a factor of $\sim 4x10^4$ (at ~0.8kV). If our results are due to the pinch effect, we are then observing the pinch effect phenomenon at the smallest spark energy reported so far in the literature, i.e., we are investigating its threshold behavior.

However, we have some doubts that the pinch effect is really understood quantitatively. The sparking phenomenon is an extremely complex process if we insist on a real quantitative evaluation of its dynamics. Its understanding is not yet at a level of that of the electron transport at low drift electric fields or small avalanches, which can be solved reasonably accurately using the three-dimensional Monte Carlo simulation [5] [the computer program follows the electrons and ions in small steps (fraction of a ps) and evaluates electrostatic forces, position and velocities of each electron and ion, and probability of various physics processes using the electron-molecule scattering cross-sections]. It is not possible to do this for sparks having large number of electrons involved in the pinch effect at this time, not only because of the computational difficulties but also because one does not necessarily know details of all physics processes involved. For example, in Chapter 4 we mention one additional possible mechanism which may have been neglected in the theory of the pinch effect, and may contribute to the X-ray production in our tests.

One practical benefit of running small spark energy is that the sparking electrodes do not wear out quickly and the device is suited for long-term investigations. The spark electromagnetic noise requires careful shielding for fast detectors. For drift chambers with a long drift, one can be easily protected by a drift time delay of about 1-2 μs. The X-rays were monitored at 90º in respect to the spark axis during all tests in this paper. An initial approximate observation indicates that they may be isotropic, although this is yet to be confirmed by a larger test detecting X-rays over a larger solid angle.

2. EXPERIMENTAL SETUP

2.1. Description of X-ray producing apparatus

Figure 1 shows schematically the spark producing apparatus. It uses a spark gap with a 1 mm gap between the points, which is placed in a small brass vessel equipped with a thin window to allow low energy X-rays to penetrate (in final tests we also used carbon electrodes in a specially prepared spark gap). The window opening is ~1.27 cm diameter and its material is either 12.7 μm stainless steel (sealed by a conducting epoxy), or 50 μm Mylar foil. The sparking vessel is connected to a vacuum pump from one side, and to a gas bottle from another side. The gas pressure is controlled by a small needle valve throttling the gas flow while pumping. The pressure is monitored by a thermocouple gauge with an accuracy of a few microns (1 μ = 10^{-3} Torr). The pump was capable of reaching a pressure (p) of 10-20 μ.

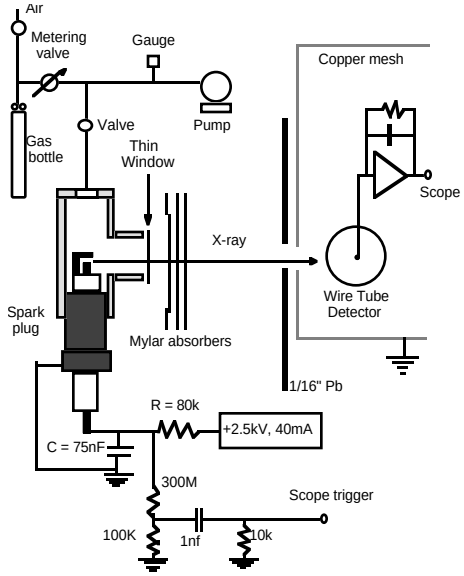

Fig. 1. Our experimental setup for sparking in gases at low pressure. It uses a spark plug with a 1 mm gap, operating as a relaxation oscillator.

The operating parameters of the spark gap were tuned to maximize the X-ray production; this occurs in a relatively narrow window of the parameter space. The spark gap operates at low

pressure between 0.2 and 1Torr, depending on the gas choice. It operates as a relaxation oscillator with a charging resistor R = 80kΩ and a charging capacitor C = 75nF. Because of excessive heating, the charging resistor R is made with an equivalent circuit involving six pairs of ~27kΩ, 10W resistors; it is necessary to cool them with a small fan. The high voltage power supply, capable of delivering up to 40 mA DC current, operates at +2.5kVDC voltage. The sparking voltage (V_{spark}) varies between 0.8 and 2.1kV, which corresponds to a spark energy ($\frac{1}{2}CV_{spark}^2$) between 0.024 and 0.17J/pulse, and a spark charge (CV_{spark}) between $4x10^{14}$ and 10^{15} electrons/spark. The spark repetition period (T) is set typically between 5 and 20ms by the choice of gas pressure, which corresponds to sparking rates between 50 and 200Hz.

2.2. Spark voltage monitoring

First, we calibrated the DC power supply output with a precision voltage divider and a digital voltmeter. This resulted in a small ~0.6% correction. Second, we calibrated a spark voltage V_{spark} relative to a spark period T using a special voltage divider, as shown in Fig.2a. To monitor the varying voltage with a voltage divider, it is necessary to compensate the resistors for their parasitic capacitance. This was done by measuring a parasitic capacitance of the 300MΩ resistor in Fig.2a, and then empirically tuning the 80nF capacitor to minimize an undershoot in the monitored voltage of Fig.2b. The monitored voltage of Fig.2b was used to determine a correlation between the sparking voltage V_{spark} and a sparking period T of the oscillator. By measuring the sparking period T, one can uniquely determine the sparking voltage V_{spark}, which is shown in Fig.2c. Finally, we have also used a spark gap[1] CG3-1.5 to calibrate V_{spark}. Its sparking voltage was selected to be 1.4kV. For V_{spark} < 1.4kV, the spark gap did not fire. This was a simple way to confirm that our calibration is correct, and that there is no fast transient exceeding V_{spark}.

The relaxation oscillator has the following feature: for a given spark gap distance d, gas pressure p and gas choice, the sparking voltage V_{spark} is determined according to Paschen's law, which says that V_{spark} is a function of pd. We operated in a region of the law where increasing the pressure reduces the sparking voltage, which in turn reduces the sparking period T.

During the experiment, we would typically monitor the sparking period, which is easy to measure, and use the calibration curve of Fig.2c to obtain the corresponding sparking voltage. Depending on the choice of the gas pressure in a given gas, we would typically select the sparking voltage V_{spark} between 0.8 and 2.1kV during this experiment, while running the high voltage power supply always at a constant value of +2.5kV. We used the scope triggering circuit, described in Fig.1, to determine the sparking frequency T.

---

[1] Made by General Instrument Co., Chicago, Il 60645, U.S.A.

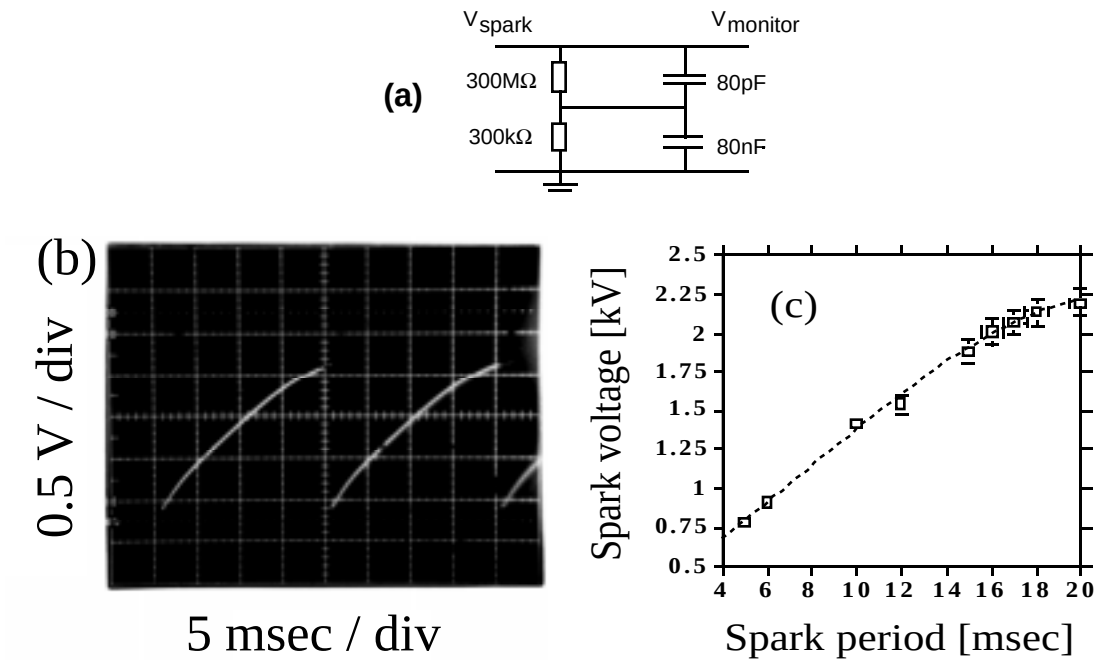

Fig. 2. We used a special voltage divider (a), equipped with a capacitive correction, to determine a sparking voltage V_{spark} and a sparking period T (b). A calibration curve correlating the sparking voltage V_{spark} and the park period T is shown in (c).

2.3. X-ray detectors

We have used four types of X-ray detectors during this test: a Geiger detector TBM-3S[2] , a single wire proportional tube detector, a long drift detector, and the YAP scintillator[3] coupled to the XP2230 photomultiplier[4] . The most prominent systematic effect was the spark noise generated by the spark gap located very close to the detector. To limit its influence, we have constructed a large copper mesh Faraday cage around the detector, the connecting cables were placed in the grounded copper pipes, and the spark gap vessel and its high voltage connection was well grounded. The signal detection in the wire tube detector and the YAP scintillator occurs during the largest spark noise, and therefore, it was necessary to place them in the second local coaxial shield. The easiest way to eliminate the spark noise was with the long drift detector because in this particular geometry one can easily separate the spark noise from the X-ray signal by a choice of a suitable electric drift field. In all cases, it was easy to verify that we indeed detect the X-rays by placing an absorber between the spark plug vessel and the detector window.

---

[2] Made by Technical Associates, Canoga Park, CA 91303, U.S.A

[3] YAP stands for $YAlO_3$:Ce; density 5.37 g/cm^3, peak emission at 370nm, typically 3-4 p.e./keV.

[4] Made by Amperex, North American Philips Co.

The Geiger detector TBM-3S is a commercially made battery operated detector equipped with a thin Mylar window of a 1.5 mg/cm^2 thickness and 5 cm diameter. It is filled with halogen gas.

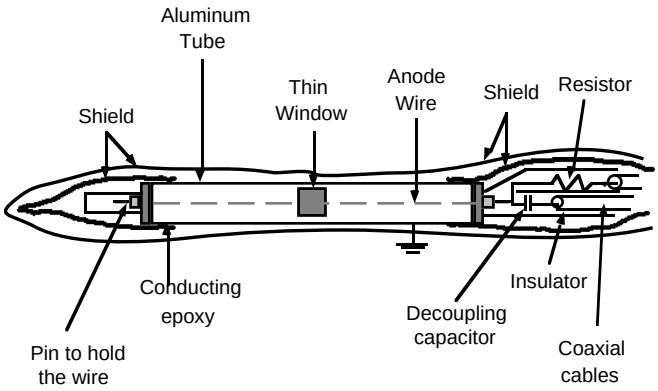

Fig. 3. Geometry of the single wire proportional tube detector including its spark noise shield.

Figure 3 shows the geometry of the wire tube detector. The gold plated tungsten anode wire diameter is 38 μm. The aluminum tube has 10 mm i.d. with a 1 mm wall thickness. The tube has a 10 mm x 10 mm opening in the center, which is covered with a 30 μm thick aluminized Mylar foil. The foil is connected electrically to the tube wall with conducting epoxy and sealed with a DP-190 epoxy. The detector is operating with a 95% Ar+5% CH_4 gas mixture at 1 atm pressure. This choice was primarily motivated by its nonflammability.

Figure 4 shows the geometry of the long drift wire detector. The drift cell is made of two sections: a drift region made of equally spaced stainless steel rings and a gain region containing 20 μm gold plated anode wires surrounded by a nickel plated cathode. The drift field is defined by the potentials V_1 and V_2. The resistor chain provides voltages to the individual stainless steel rings. The value of each resistor is 10MΩ. The drift region has a cylindrical shape with 2.5 cm i.d. and 12 cm long active volume. The entrance window into the long drift detector is made of ~13 μm thick aluminized Mylar foil. The gas gain is controlled by the cathode voltage V_C. All anode wires are connected together to a single amplifier. The detector also operates with a 95% Ar+5% CH_4 gas mixture at 1 atm pressure. To be insensitive to a spark noise, we would typically choose a drift field of only ~8-10V/cm corresponding to a very low electron drift velocity of ~5mm/μs. Typically, with this detector, the spark noise would appear only in the first 1-2 μs after the scope trigger, followed by a perfect noise-free period. We would then observe events of interest between 3 and 25 μs after the scope trigger.

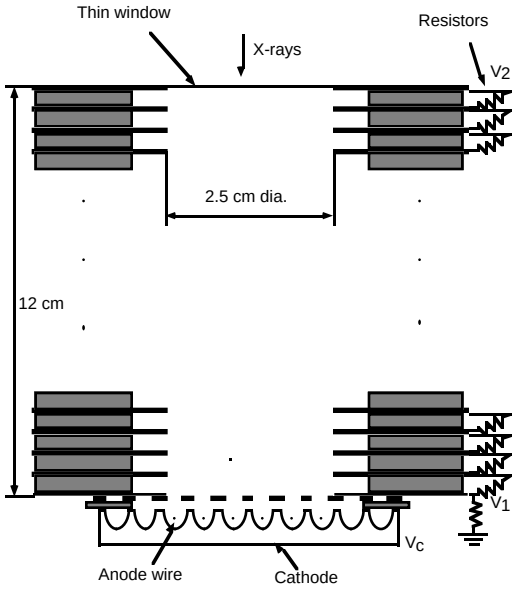

Fig. 4. Geometry of the long drift detector.

The YAP scintillator was a cube (1cm x 1cm x 1cm) coupled to a XP2230 PM tube with a UV coupling grease. A good light collection was ensured by covering the sides of the scintillator with Teflon tape; the light leak was stopped with two layers of black paper tape. Because we used an amplifier with a large gain (~15mV/pC), the photomultiplier tube (PM) operated at a very low voltage of -1.4kV. The main reason to use this detector was to investigate the high energy end (tens of keV) of the pulse height spectrum, where the gaseous detectors start loosing efficiency.

2.4. Electronics used in the test

The long drift detector was used to measure the multiplicity of the X-ray bursts. Its amplifier was a battery operated charge sensitive amplifier with a gain of ~15mV/pC, a shaping time of ~65ns, and σ_{noise}~2000 e^-. This sensitivity is enough to be able to detect even single electrons arriving on the wire, assuming that the gas gain is in the range of 10^5. A conversion of a 3-10keV X-ray generates a much larger signal, equivalent to several hundred electrons.

The wire tube detector measured the X-ray pulse height spectra using two methods: (a) peak sensing method using a LeCroy TRA100 amplifier with a gain of ~50mV/pC and a shaping time of ~20μs, together with a digital oscilloscope (reading individual pulses manually), (b) charge sensing method using the battery operated amplifier (see above) with the pulse height analyzer LeCroy QVT 3001 in q-mode operating with an external 400ns long gate (the YAP scintillator detector was also using this method).

2.5. Expected X-ray attenuation factors and detection efficiency

Figures 5a and 5b show calculated attenuation curves for various materials and an expected detection efficiency for the tube and long drift wire detectors.

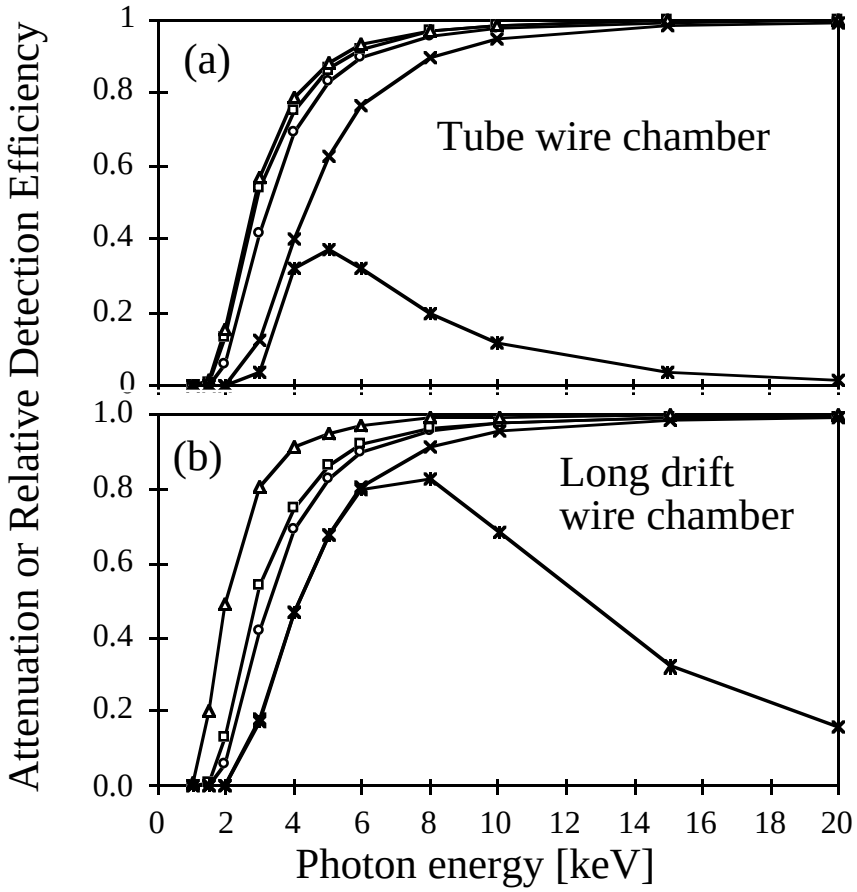

Fig. 5. Calculated attenuation N/N_0 curves for various materials in the X-ray path, and expected X-ray detection efficiency for (a) the tube wire chamber and (b) the long drift detector. The attenuation was calculated for 51 μm thick Mylar sparking vessel window (open circles), 3 cm of air (squares), 33 μm (tube) or 12.5 μm (long drift) wire chamber window (triangles), the combined attenuation factor (x) and the final detection efficiency (star).

The attenuation factor is defined as $\eta(E) = N/N_o = \exp(L/L_o)$, where L is the X-ray path length and L_o is the attenuation length calculated from the absorption coefficient in a given material [6]. The X-ray detection efficiency, $\varepsilon(E)$, defined as a ratio of detected and produced number of X-rays, was calculated as follows:

$$\varepsilon(E) = \eta_{mylar}(E)\,\eta_{air}(E)\,\eta_{window}(E)\,(1-\eta_{gas}(E)) \qquad (1)$$

where η_{gas} is the attenuation in 95% Ar+5% CH_4 gas mixture, and other factors are the attenuation factors in the materials in the X-ray path. We assume that the wire chamber detection efficiency is

close to 100% for a charge generated by the X-rays. From Fig.5b, one can see that the long drift detector has a good X-ray detection efficiency between 3 and 20keV.

3. EXPERIMENTAL RESULTS

We have observed X-ray production with all four types of detectors described in Section 2.3. There are three arguments for this statement: (a) the radiation was not affected by a strong magnet placed between the sparking vessel and the detector, indicating that we are indeed dealing with the X-rays or neutral particles; (b) the range measurements are very consistent with the X-ray production; (c) the response from the gaseous detectors strongly indicates soft X-ray production (pulses are comparable in size and shape to pulses from an Fe^{55} X-ray source). The X-rays were monitored at 90^{o} in respect to the spark axis during all tests in this paper.

3.1. Observation of X-ray showers

The most convincing proof of the existence of the X-ray bursts in a single event came from the long drift detector. The long drift detector operating condition was described in Section 2.3. A fraction of the solid angle extended by the sensitive region of the long drift detector in this test was $\Delta\Omega/\Omega$~0.0019. Fig.6a shows oscilloscope pictures of the X-ray events, which follow the initial spark noise. The relaxation oscillator was operating in air at V_{spark}~1.45kV and p~270 μ.

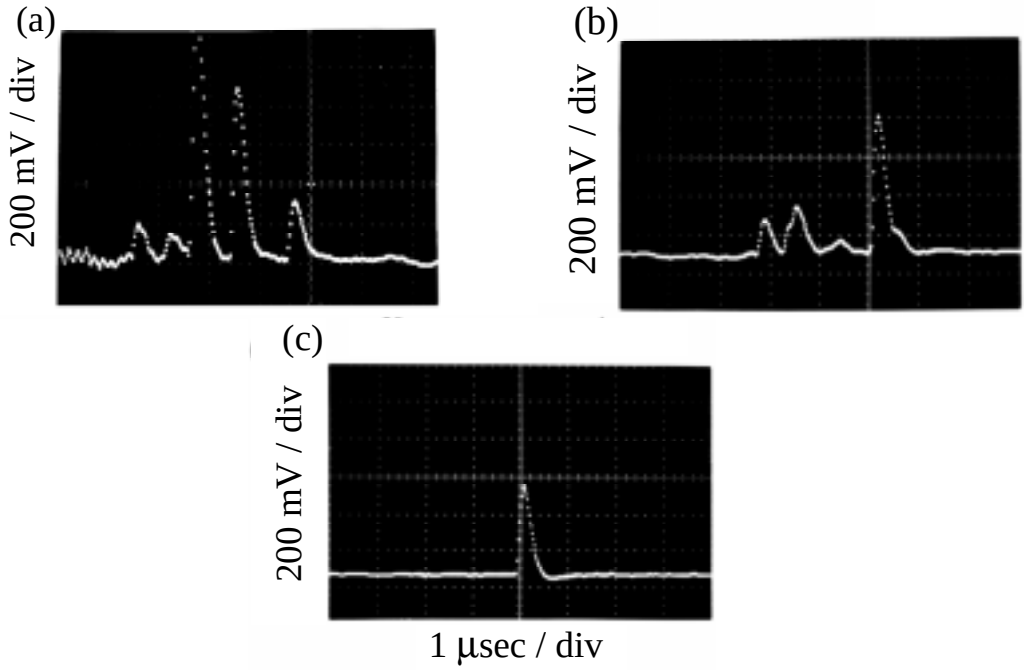

Fig. 6. (a) A cluster of X-ray pulses detected in the long drift detector; sparking in air at a sparking voltage V_{spark} ~1.45kV and a pressure of ~270 μ; (b) A cluster of X-ray pulses detected in the long drift detector; sparking in argon at a sparking voltage V_{spark}~2kV and a pressure of ~170 μ; (c) A calibration pulse from an Fe^{55} X-ray source for the same gas gain.

Figure 6b shows similar X-ray production with argon at V_{spark}~2kV and p~170μ. For comparison, Fig. 6c shows a typical calibration pulse from the Fe^{55} X-ray source. Notice that the X-ray events appear in clusters (Figs. 6a and b). To study the single X-ray events, it is necessary to adjust their flux so that the probability to observe the X-ray pulse per spark was only ~5%, thus ensuring only a small probability of a pile-up from different events. This is achieved by placing an additional 178μm Mylar absorber in the X-ray path, creating a total Mylar thickness of 261μm between the spark and the sensitive volume of the long drift detector. The sparking vessel is filled with argon, and operates at V_{spark}~2kV and p~170μ. The counting of X-ray pulses is done visually using a digital scope. Fig.7 shows a multiplicity distribution of the X-ray pulses per spark, indicating a mean of three. Extrapolating this result to a 4π-solid angle and assuming an isotropic distribution, one would expect more than $3*(\Omega/\Delta\Omega)$~1500 X-ray pulses.

From a visual observation of scope traces, it appears that the average energy of the X-rays is below ~10keV. The signal disappears when placing either a 1.6mm thick lead sheet or even a 762μm thick Mylar sheet in front of the long drift detector (see the next chapter for a quantitative evaluation of average energy).

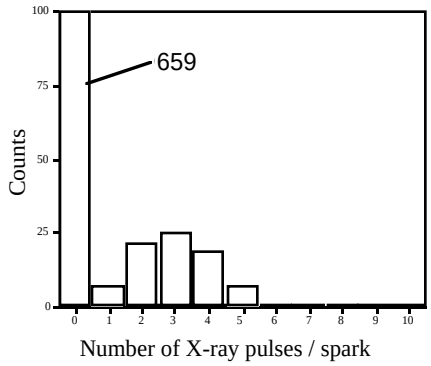

Fig. 7 An average X-ray multiplicity per spark in argon, sparking voltage V_{spark}~2kV and pressure of ~170μ.

The X-ray energy was between 3 and 10keV on average, and probability to observe an X-ray pulse per given spark was kept at only ~10% to ensure a proper X-ray counting.

3.2. Average effective X-ray energy using a range measurement

An advantage of the range measurement is that it is simple and insensitive to any spark noise. We have used Mylar, Kapton, aluminum, and stainless steel absorbers mounted into slide frames. The slides were carefully placed into an X-ray path between the sparking vessel and the detector. Fig. 8a shows a comparison of calculated and measured attenuation curves for the setup using the Geiger counter TBM-3S. The X-rays passed through a 12.7μm thick stainless steel sparking vessel window, 3 cm of air and 38μm of Mylar foil on the counter. The sparking vessel was operating with air at V_{spark}~2.1kV and p~240μ. One can see that an average measured effective

energy of X-rays is slightly above 4keV. Fig.8a also shows the measured calibration data using the Fe^{55} source producing 5.9keV X-rays; it agrees fairly well with the calculation.

Fig.8b shows a comparison of the calculated and measured attenuation curves for the setup using the tube wire detector. In this case, the X-rays passed through a 12.7 μm thick stainless steel sparking vessel window, 3 cm of air, and a 30 μm thick aluminized Mylar foil of the tube window. The sparking vessel was operating with air at V_{spark}~2.1kV and p~240 μ. Again, one can see that an average effective energy of X-rays is slightly above 4keV. Fig.8b also shows the calibration data using the Fe^{55} source producing 5.9keV X-rays. Both methods, one using the Geiger counter and one using the tube wire detector, agree with each other.

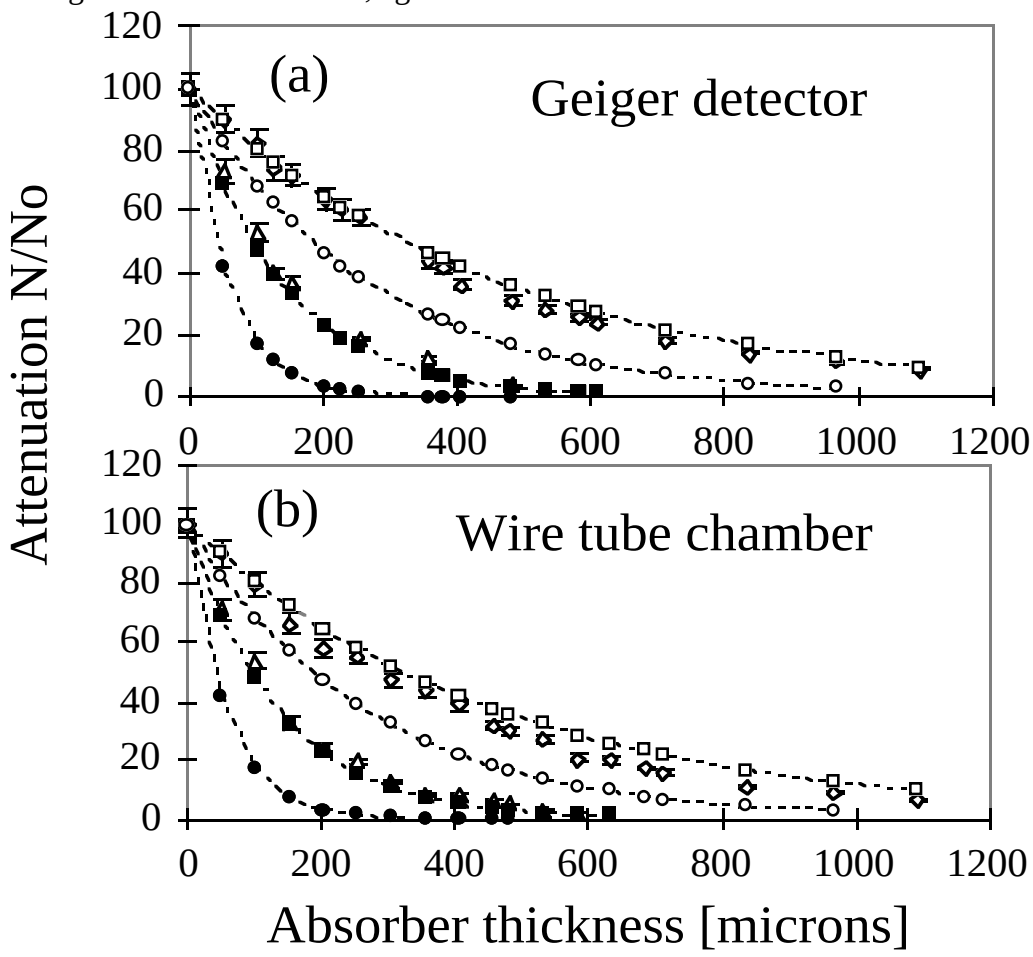

Fig. 8 (a) A comparison of a range measurement and calculated attenuation curves using the Geiger counter TBM-3S. The sparking data (open triangles) were obtained with air at sparking voltage V_{spark} ~2.1kV and pressure of 240 μ, calibration was done using the Fe^{55} X-ray source (open diamonds), the calculation was done at 6keV (open squares), 5keV (open circles), 4keV (filled squares), and 3keV (filled circles). (b) The same for the tube wire detector; the sparking vessel was operating with air at sparking voltage V_{spark}~2.1kV and pressure of 240 μ.

The spark charge contains approximately ~10^{15} electrons. The question is, what is the probability that one such electron creates an event, containing any number of X-ray pulses. Combining the results from the long drift detector of Sections 3.1, and the tube detector of Section 3.2, we calculate this probability as follows: ~$0.1*5*10^{-15} = 5x10^{-16}$, where 0.1 is the probability to observe an X-ray even per spark containing 10^{15} electrons, a factor of 5 comes from the absorption correction caused by the 262 μm Mylar absorber in the X-ray path (see the multiplicity measurement in chapter 3.1), assuming an average X-ray energy ~4keV - see Fig.8b. To be able to see this phenomenon one needs a very large instantaneous spark current (>400A). For example, one would not see it using electrons from an ordinary β-source.

3.3. X-ray energy distribution

The difficulty to correctly measure the pulse height distribution in this experiment is mainly related to a short duty cycle of the X-ray production, and to a spark noise. The X-rays are produced within ~150-200ns time interval (see Section 3.5), and they seem to occur in multiple events (see Section 3.1). To assure that we are dealing predominantly with the single X-ray pulses when measuring the pulse height spectra, we need to limit the probability of a single X-ray pulse per spark to less than 5%. This is achieved by (a) restricting the X-ray flux with a ~1mm diameter hole in the 1.5mm thick lead sheet, and (b) by running at the lowest possible sparking voltage. Despite these precautions, there is still a nonzero chance of having two X-ray pulses within the integration gate, and therefore, one should not over-interpret a maximum X-ray energy measured in the test. The maximum observed energy is also affected by a resolution of the detector, which has to be determined by a separate calibration run. The spark noise was reduced by using careful shielding precautions (see Section 2.3), and by running relatively long shaping time of the amplifier, which, however, made it more difficult to resolve doubles.

3.3.1. Wire tube detector with a long integration time constant.

We use a charge integrating amplifier with a gain of ~50mV/pC and a shaping time of ~20 μs, and a digital oscilloscope to measure the pulse height spectrum by determining a peak of each pulse. In this way, every pulse contributing to the pulse height spectrum is visually checked. The X-rays pass through a 51 μm thick Mylar window of the sparking vessel, 3 cm of air and a 30 μm thick aluminized Mylar foil of the wire tube window before there is a detection in the wire tube chamber operating with 95% Ar+5% CH_4 gas.

Figure 9a shows the uncorrected X-ray pulse height spectra in air, hydrogen, argon, and xenon gases. The spark gap operates at V_{spark}~0.9kV and p~310 μ for air, at V_{spark}~1.55kV and p~950 μ for hydrogen, at V_{spark}~0.8kV and p~240 μ for argon, and at V_{spark}~1.81kV and p~135 μ for xenon.

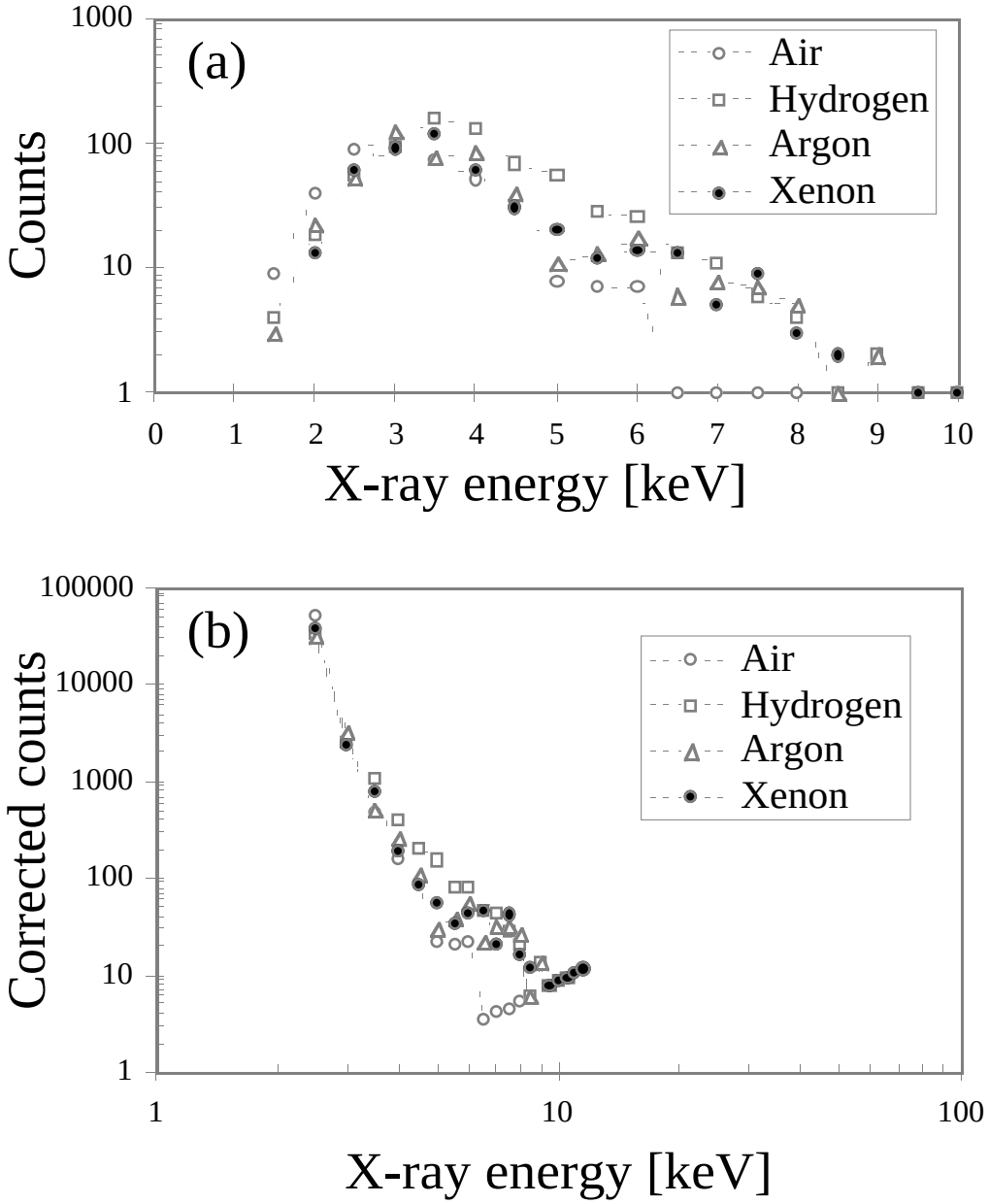

Fig. 9. (a) A measured X-ray pulse height spectrum using the wire tube detector while sparking in air at ~0.9kV; hydrogen at ~1.55kV; argon at ~0.8kV; xenon at ~1.81kV. The X-rays pass through the 51 μm Mylar window in the sparking vessel, 3 cm of air, and a 30 μm thick aluminized Mylar foil in the wire tube chamber. The energy scale is calibrated using the Fe^{55} source; the resolution σ/Peak of the wire tube detector is ~14% at 5.9 keV. (b) The same pulse height spectra as shown in Fig. 9a, but corrected for the attenuation factors in various materials and the wire tube X-ray detection efficiency - see Fig.5a.

Using the calculated attenuation factors for each absorber in the X-ray path, and using the calculated wire tube detection efficiency based on the energy dependent attenuation factors in each component of the chamber gas (see Eq.1, Ref.6, and Fig.5a), one can correct the measured spectra of Fig.9a and obtain a shape of the primary X-ray spectra at the source. Fig.9b shows the final results for air, hydrogen, argon, and xenon in the sparking vessel. The spectra have the same shape within the experimental errors and they follow a power law distribution.

The scale is calibrated with the Fe^{55} radioactive source. The resolution σ/Peak of the wire tube detector is ~14% at 5.9 keV.

3.3.2. Wire tube detector with a short integration time constant

In this test, the wire tube detector is coupled to the charge integrating amplifier with a gain of ~15mV/pC and shaping time of ~65ns. The pulse height spectrum is measured using the QVT pulse height analyzer operating in the charge integrating mode (q-mode) with an external gate of 400ns long. The shape of the X-ray distribution and the maximum energy observed in argon and xenon are consistent with the results presented in Fig.9a.

3.3.3. YAP scintillation detector with a short integration time constant

In this test, the YAP scintillation detector is coupled to a PM operating at -1.4kV. The PM anode output is amplified by the charge integrating amplifier with a gain of ~15mV/pC and the shaping time of ~65ns. As indicated above, the pulse height spectrum is measured using the QVT pulse height analyzer operating in q-mode with a 400ns long external gate.

In this case, we are interested to see if there are some X-rays with much larger energies than ~10keV. Fig.10a shows the uncorrected X-ray pulse height spectrum in xenon on the logarithmic scale. The spark gap was operating at V_{spark}~1.81kV and p~135μ. Fig.10b shows the same spectrum, but in this case the X-rays are blocked with 1.5mm thick lead sheet. As expected, no events are observed above the pedestal peak. Fig.10c shows the calibration spectrum using the Cd^{109} radioactive source. The resolution σ/Peak of the YAP detector is only ~26% at 22 keV, which is expected due to the finite photoelectron statistics for this type of scintillator. This resolution is considerably worse compared to the gaseous wire tube detector. Taking into account the relatively poor resolution of the YAP detector, we conclude that the result of this measurement is consistent with the corresponding result from the wire tube detector in Fig. 9a. However, Fig.10a shows few events with energy up to 20-25keV, which would indicate a presence of larger energies compared to what we measured with the gaseous wire tube detector in Fig.9 (at X-ray energy of ~20keV the gaseous detector has practically zero detection efficiency - see Fig.5a).

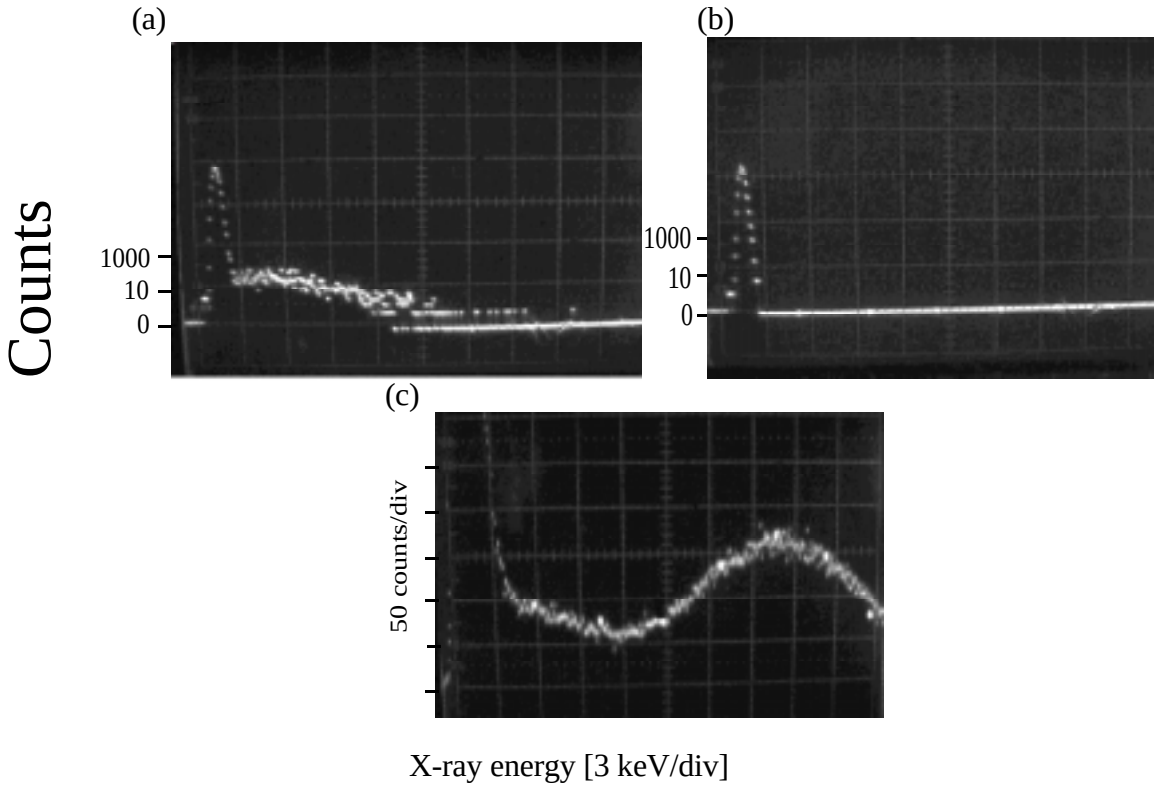

Fig. 10. (a) A measured X-ray pulse height spectrum using the YAP scintillation detector while sparking in xenon at ~1.81kV. The X-rays passing through the 51 μm Mylar window in the sparking vessel, 3 cm of air, and a 30 μm thick aluminized Mylar foil in the wire tube chamber (log vertical scale). (b) The same but the X-rays blocked with 1.5mm thick lead sheet (log vertical scale). (c) The calibration with a Cd^{109} radioactive source producing 22keV X-rays; the measured resolution σ/Peak is ~26% at 22 keV (linear vertical scale). Every 50-th count is bright.

3.4. X-ray production rate as a function of E/p, sparking voltage and gas

In this test, the X-rays pass through a 51 μm thick Mylar window of the sparking vessel, ~3cm of air, and the Geiger detector window (38 μm thick Mylar), i.e., the X-rays below 2-3keV were absorbed. We placed additional Mylar absorbers in front of the detector to evaluate the hardness of the X-ray radiation. The gases in the sparking vessel were hydrogen, air, nitrogen, argon, and xenon. We used the following gas pressure ranges: 195-230 μ for argon, 120-140 μ for xenon, 280-320 μ for air, 275-330 μ for nitrogen, and 850-1020 μ for hydrogen. Outside these pressure ranges the X-ray production stopped, although the spark gap continued to glow. Fig.11 shows the measured X-ray rate in the Geiger detector as a function of the sparking voltage for several gases in

the sparking vessel. Notice that the argon X-ray spectrum appears to be hardest in this group of gases.

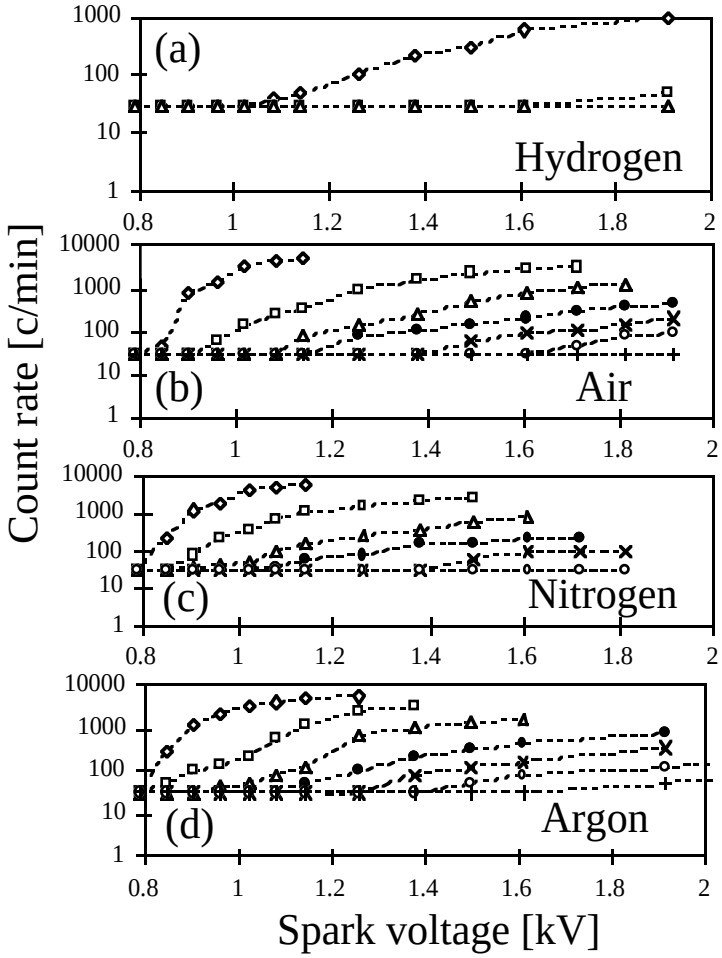

Fig. 11. The rate of the X-rays in the Geiger detector as a function of the sparking voltage V_{spark}, gas and a Mylar absorber thickness: for (a) hydrogen, (b) air, (c) nitrogen and (d) argon; no absorber (diamond) and Mylar absorbers of the following thickness: 127 μm (square), 254 μm (triangle), 356 μm (filled circle), 483 μm (x), 610 μm (filled circles), and 711 μm (cross).

Many gaseous phenomena depend on the E/N variable, where E is the electric field and N is the number of molecules per cm^3. E/N is often approximated by an E/p variable, where p is the gas pressure. For example, the electron drift velocity is often expressed as a function of E/p. Unfortunately, it is difficult to know E precisely due to a dynamic behavior of the spark; the space charge effects must also be very important for charges of ~10^{15} electrons per spark; for E/p higher than 10kV/cm/Torr, the electron energy is higher than ~50eV, causing ionization. Similarly, a

spark pressure may not be known since it depends on the spark temperature, which is not directly measured during the test (a surface temperature of the sparking vessel is increased rapidly; within 30 minutes it climbed to 70-80ºC). Therefore, only approximations can be made. We assume that $E = V_{spark}/d$, where V_{spark} is determined from Fig.2c, d is ~1 mm, and p is the gas pressure monitored ~20cm away from the sparking vessel.

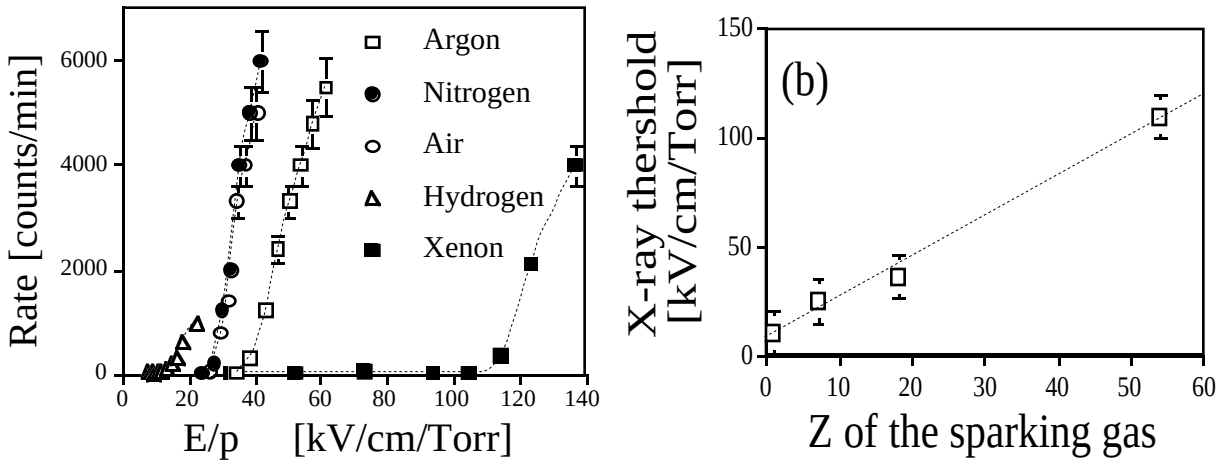

Fig. 12. (a) The production threshold and the rate dependence of the X-rays in the Geiger detector on the E/p value of the gas in the sparking vessel. (b) The dependence of the X-ray production threshold on the atomic number Z of the gas in the sparking vessel.

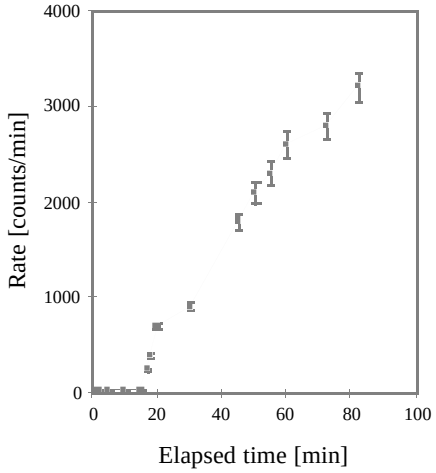

Fig. 13. The measured X-ray production rate as a function of elapsed time (sparking in air at V_{spark}~0.9kV). The increase is due to the gas heating, which changes E/p.

Figure 12a shows the measured the X-ray rate in the Geiger detector as a function of the E/p value for several gases in the sparking vessel. In this measurement, no additional absorber was

placed between the sparking vessel and the detector. One can see that hydrogen starts producing the X-rays at the lowest E/p, xenon at highest. From Fig.12b it appears that the X-ray production threshold correlates with the atomic number Z of the gas.

Figure 13 shows the result in air at sparking voltage V_{spark}~0.9kV. We see an increase in the rate as a function of elapsed time since the beginning of the sparking. This may be related to an increase in the sparking temperature which changes E/p.

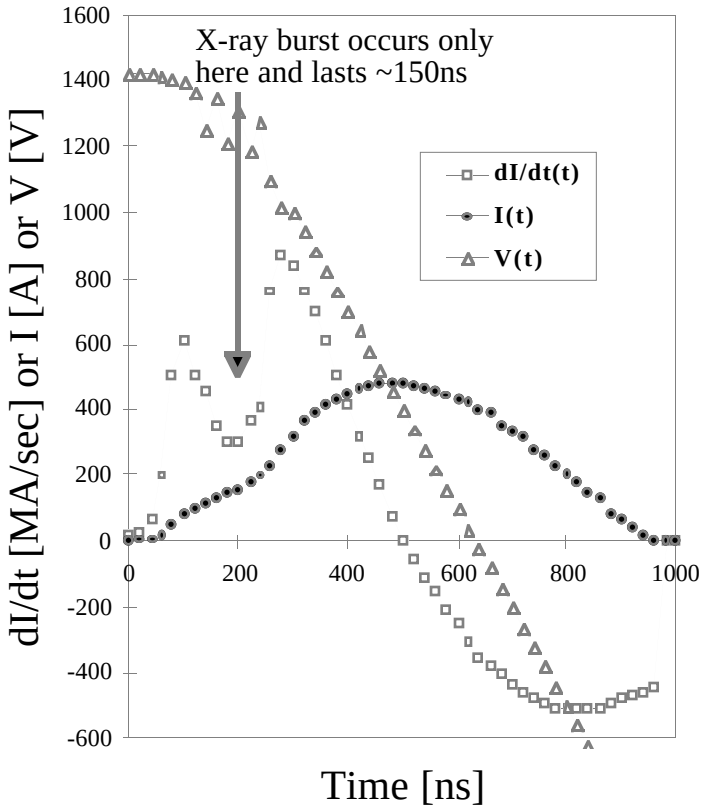

Fig. 14. Measured time development of the current I(t), voltage V(t), and current derivative dI/dt(t) relative to the X-ray production during our sparking tests. The X-ray burst duration is ~150-200ns, and is observed at ~200ns after the spark starts. The spark gap is operating, in this case, in air at V_{spark}~1.4kV and p ~290 μ; similar shapes were measured at V_{spark}~0.9kV.

3.5. The X-ray production and the I, V, and dI/dt dependence of the spark

We have added several components to the setup of Fig.1 in order to measure the I(t), V(t), and dI/dt(t) spark parameters. The current I(t) is measured with a 1.2 Ω shunt resistor placed in the ground return of the spark gap, the voltage V(t) is measured with a simple 1000:1 divider, and the current derivative dI/dt(t) is measured using the toroid coil (so called Rogovski coil [7]). The coil is

placed around a conductor delivering the current into the spark gap; it has 30 turns, a minor radius of 4.2mm, and a major radius of ~17.8mm. To check the Rogovski coil measurement, we also performed a numerical derivative of the I(t) curve. Fig.14 shows time development of the current, voltage, and dI/dt during the spark and the relative timing of the X-ray production. The X-rays were measured in the wire tube or the YAP detectors.

We observe the first X-rays at ~200ns after the spark starts and are all contained within a time interval lasting 150-200ns, which corresponds to an observation of a slight dip in the current I(t). The current dip also corresponds to the largest swing of the dI/dt(t). The voltage measurement shows a small ripple effect at this time; however, we do not measure larger values than the expected spark voltage V_{spark}. The observation of the X-ray production during the dip in the current appears to be consistent with what has been observed during the pinch effect studies [1-4].

4. DISCUSSION OF THE PRODUCTION MECHANISM OF THE X-RAYS

We clearly see the production of soft X-rays with energies between 2 and 10keV, which are above the expected value given the known sparking voltage. The effect occurs during a slight dip in the current I(t). This observation appears to be consistent with the earlier pinch effect studies [1-4], which are explained in the plasma field literature using the theory of radiation collapse [1].

However, one should stress that our spark energies at our smallest sparking voltage (~0.8kV) are at least a factor of ~$4x10^4$ smaller compared to the spark energies used in Refs.1-4. If our results are due to the pinch effect, we are then observing the pinch effect phenomenon at the smallest spark energy reported so far in the literature, i.e., we are investigating its threshold behavior. The maximum observed X-ray energy (~10keV), generated at the lowest voltage (~0.8kV), is ten times more than expected; it is above the K-shell energy for gases used in our tests, or the materials used in our spark electrodes (see Table 1 and Chapter 4). The X-ray production persists even for the carbon electrodes, which have the smallest K-shell energy (0.284keV); this would appear to eliminate the theory that the electrode atoms are responsible for the X-ray production. Furthermore, we have evidence that the production threshold and the X-ray rate is dependent on the gas choice in the sparking vessel. Because of the doubts that the pinch effect is the only explanation for the observed phenomenon, we were interested in searching for other possible explanations:

(a) The first obvious question is, if our spark voltages could produce the characteristic K-shell X-rays in the materials or gases which are present in our system, assuming a multi-electron participation on a liberation of a K-shell electron of some heavy atom such as iron, nickel, or molybdenum (see Table 1). The phenomenon would be similar to the multi-photon ionization of the gas impurities observed when a UV laser is shining into a gaseous drift chamber. However, it appears that such a production is very unlikely. It is difficult for a charged electron, having an

energy of only 50-100eV, to deeply penetrate inside the atom (compared to a neutral photon during the multi-photon excitation).

Table 1 - Characteristic X-ray energies in keV of some elements which could exist in the vicinity of the spark, either in the gas or on the surface of the electrodes (a primary element or contamination); data obtained from the Handbook of Chemistry and Physics, published by the Chemical Rubber Co., Cleveland, Ohio, 1971, page E-178.

Z	Element	K	L_1	L_2	L_3	M_1	N_1
6	Carbon	0.284					
7	Nitrogen	0.400					
8	Oxygen	0.532					
13	Aluminum	1.556	0.087	0.072			
14	Silicone	1.838	0.118	0.0077			
15	Phosphorus	2.142	0.153	0.128			
17	Chlorine	2.822	0.238	0.202	0.201	0.0297	
18	Argon	3.200	0.287	0.246	0.244	0.035	
20	Calcium	4.038	0.399	0.350	0.346	0.0471	
22	Titanium	4.966	0.530	0.462	0.456	0.0605	
24	Chromium	5.988	0.679	0.584	0.574	0.0762	
25	Manganese	6.542	0.762	0.656	0.644	0.0817	
26	Iron	7.113	0.849	0.722	0.709	0.0937	
28	Nickel	8.337	1.02	0.877	0.858	0.111	
40	Zirconium	17.998	2.533	2.308	2.224	0.432	0.0516
42	Molybdenum	20.003	2.869	2.630	2.525	0.509	0.0692
54	Xenon	34.551	5.448	5.103	4.783	1.14	0.208

To eliminate this possibility experimentally, we decided to use the carbon electrodes in the spark gap. The insulator is made of nylon to eliminate the porcelain,[5] which could in principle contain some ferro-electric crystals. We repeated the production of the soft X-rays with this setup under similar experimental conditions, as has been discussed in this paper. This indicates that the soft X-

[5] According to Dr. B. Manning of Champion Co., the porcelain in their spark plug (J-12Y) does not contain the ferro-electric crystals. The spark plug electrodes are made of Ni, Cr, Ma, Si, Ti, Zi alloy and traces of C and Fe; the ceramic insulator is made of Al_2O_3 (~90%), and the glass phase is made of clay containing Ti, Ca, Na, Fe, Zi, etc., impurities).

ray production is very likely related to the gaseous phenomenon and not to the spark gap material, or to the insulator properties.

(b) In principle, the hot plasma can excite the X-rays through the "thermal Bremsstrahlung" phenomenon, which is caused by the electron-ion collisions at extremely high temperatures. It is necessary to heat the plasma to temperatures between 10^7 and 10^8 ^oK to excite the X-ray spectra seen in Fig. 9b. We exclude this possibility in our experiment because the predominant radiation from the spark is in the visible spectrum, and therefore, the average temperatures are very likely below 10^4 ^oK.

(c) One also cannot exclude that there is new physics, which goes either in parallel to the theory of the pinch effect, is driven by it, or even drives it. Refs. 8-12 suggest that both relativistic Schroedinger and Dirac wave equations allow atoms to have additional energy levels (so called Deep Dirac levels or DDL levels, which correspond to electron orbits close to the nucleus). Indeed, if such atomic levels exist then the plasma environment of the spark may be an ideal place to excite such transitions, because of a large number of ions and energetic electrons involved. A free energetic electron, perhaps even driven by the pinch effect, may enter an ion with such a velocity that it is captured by the new DDL atomic energy level. During such entry to the DDL level, the electron will radiate the Bremsstrahlung spectrum involving many photons, some of them would be X-rays (for example, the total energy released for hydrogen is close to ~509keV). One should mention that we have not observed any peaks in the X-ray energy distributions.

So far, we have not established proof that the DDL atoms exist. However, we continue this search and have finished building a larger detector capable of detecting soft X-rays over a larger solid angle. The aim of this search is two-fold: (a) to verify that the X-ray production is indeed isotropic, which must be an essential characteristic of the DDL atomic transitions (as opposed to the pinch effect), (b) to make a better estimate of the total energy sum per single event.

One may apply the results of this work to explain the soft X-ray spectra from various stars. For example, Fig. 15a shows a recent astronomical data of the X-ray flux originating from an object called PKS2155-304 as measured by the BeppoSAX satellite, equipped with the soft X-ray detectors [13]. Fig.15b shows the background spectrum from the Crab Nebula, which is used for normalization. Ref.13 speculates that the origin of these spectra is the Synchrotron emission. However, it is possible to explain, at least in principle, that the shape of the spectrum showed in Fig.15a is made of a composition of spectra similar to those shown in Fig. 9b from many contributing elements, i.e., using the plasma processes similar to those investigated by this work, as the origin of the soft X-rays from these objects.

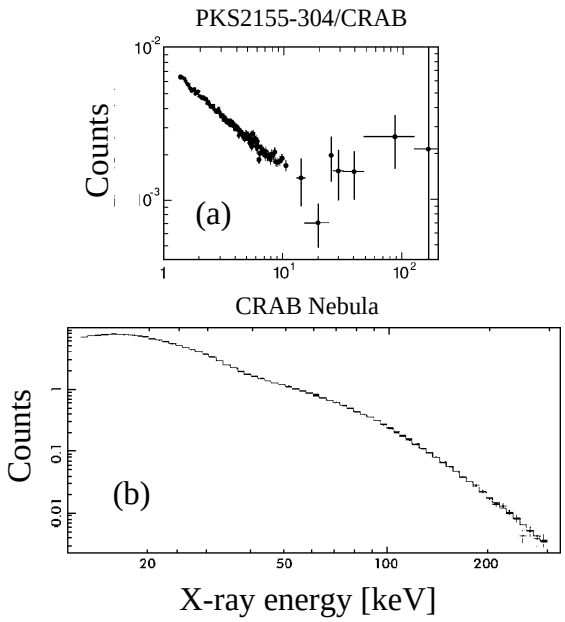

Fig. 15. (a) The recent astronomical data of the X-ray flux originating from an object called PKS2155-304 as measured by the BeppoSAX satellite, equipped with the soft X-ray detectors [8]; (b) the same for the CRAB Nebula, which is used for the normalization purpose in (a).

CONCLUSIONS

1. We observe the production of soft X-rays of energy 2-10keV by sparking in hydrogen, air, nitrogen, argon, and xenon gases at low pressure with a sparking voltage as low as 0.8-1.6kV.
2. The X-ray events appear to come in clusters, with an average mean multiplicity of 3 per event into the solid angle of our long drift detector. The extrapolated production into a 4π-solid angle is more than ~1500 pulses, assuming the isotropic distribution.
3. The X-ray pulse height spectra in all tested gases have similar shapes resembling a power law distribution between 2 and 10 keV. Using the range method, the average measured X-ray energy is about 4keV.
4. The X-ray production threshold depends on E/p of the spark chamber gas. The threshold value increases as the gas Z increases.
5. The X-ray production persists even for the carbon electrodes; this would appear to eliminate the theory that electrode atoms are responsible for X-ray production.
6. We calculate that the probability to produce an X-ray event per one electron in a given spark is less than ~5×10^{-16}. To observe this phenomenon, one needs very large currents. One would not see it with electrons from an ordinary β-source.
7. The paper also suggest that the observed X-rays could originate, at least partially, from a new

process, where energetic free electrons enter ions, and are captured on the DDL levels [8-12], radiating the Bremsstrahlung spectrum involving many photons.

8. If our results are due to the pinch effect, we are then observing the pinch effect phenomenon at the smallest spark energy reported so far in the literature, i.e., we are investigating its threshold behavior.

ACKNOWLEDGMENTS

We are grateful to Catherine Maly for editing this paper. We would like to thank Dr. S. Majewski for providing the YAP scintillator for this test.

REFERENCES

[1] K.N. Koshelev and N.R. Pereira, J. Appl. Phys., 69(1991)R21.

[2] L. Cohen et al., J. of the Optical Soc. of America, 58(1968)843.

[3] E.D. Korop et al., Sov. Phys. Usp. 22(1979)727, page 729.

[4] G. Herziger et al., Phys. Lett., A64(1978)390.

[5] H. Pruchova and B. Franek, Nucl. Instr & Meth., A366(1995)385; Issue of ICFA Instrumentation Bulletin, SLAC-PUB-7376, 1997; and H. Pruchova's Ph.D. thesis, Prague Tech. Univ.

[6] E. Storm and H.I. Israel, "Photon cross-section from 1keV to 100MeV for Elements Z=1 to Z=100," Atomic Data and Nucl. Data Tables 7(1970)565.

[7] For description of the Rogovski coil see for example S. Glasstone and R.H. Lovberg, "Controlled Thermonuclear Reactions," 1960, D. Van Nostrand Co., Inc., page 164.

[8] J. A. Maly, J. Va'vra, "Electron Transitions on Deep Dirac Levels I," Fusion Technology 24, 307, (1993).

[9] J. A. Maly, J. Va'vra, "Electron Transitions on Deep Dirac Levels II," Fusion Technology 27, 59, (1995).

[10] J. A. Maly, J. Va'vra, "Electron Transitions on Deep Dirac Levels III. Electron densities in hydrogen-like atoms using the relativistic Schroedinger equation," Submitted to Fusion Technology, November 2, 1994.

[11] J. A. Maly, J. Va'vra, "Electron Transitions on Deep Dirac Levels IV. Electron densities in the DDL atoms," Submitted to Fusion Technology, September 11, 1995.

[12] J. A. Maly, J. Va'vra, "Electron Transitions on Deep Dirac Levels V. Negative energies in Dirac equation solutions give double deep Dirac levels (DDDL)," Submitted to Fusion Technology, February 8, 1996.

[13] F. Frontera et al., Proceedings of Compton GRO Symposium, Williamsburg, 1993; P. Giommi et al., Astronomy and Astrophysics, May 28, 1997.

BEAM TESTS OF THE CLEO III LIF-TEA RING IMAGING CHERENKOV DETECTOR

M. Artuso, F. Azfar, A. Efimov, S. Kopp, R. Mountain, S. Schuh, T. Skwarnicki,
S. Stone, and G. Viehhauser*
Syracuse University, Syracuse, NY 13244-1130

and

T. Coan, V. Fadeyev, I. Volobouev, and J. Ye†
Southern Methodist University, Dallas, TX 75275-0175

and

S. Anderson, Y. Kubota, and A. Smith†
University of Minnesota, Minneapolis, MN 55455-0112

and

E. Lipeles†
California Institute of Technology, Pasadena, CA 91125-0001

ABSTRACT

We present preliminary results from a test beam run of CLEO III RICH modules. The system consists of LiF radiators and multiwire proportional chambers containing a mixture of CH_4 and TEA gases. The radiators were both flat and "sawtooth." The data were taken in a beam dump at Fermilab. We will discuss the chamber stability, electronics, the number of photons observed for both radiators, the angular resolution per photon and the angular resolution per track.

---

*Supported by National Science Foundation.
†Supported by Dept. of Energy

1 Description of the CLEO III RICH System

The CLEO III RICH is based on the 'proximity focusing' approach, in which the Cherenkov cone is simply let to expand in a volume filled with gas transparent to ultraviolet (UV) light before intersecting the detector surface where the coordinates of the Cherenkov photons are reconstructed. The components of our system are illustrated in Fig. 1. They consist of a LiF radiator, providing UV photons, an expansion region, and a photosensitive detector. The angle θ_p is the polar angle of the incident particle with respect to the radiator normal, θ is the Cherenkov angle and ϕ specifies the azimuthal angle of the Cherenkov photons. Our system is based on the one developed by the College de France-Strasbourg group [1].

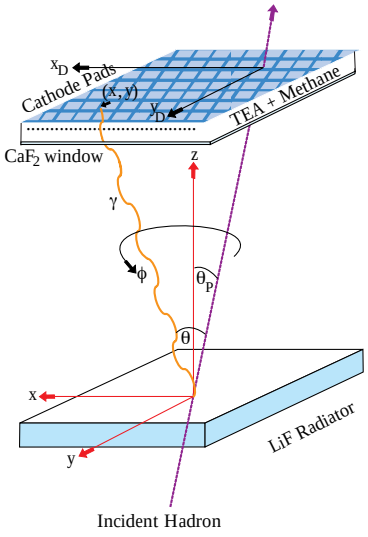

Figure 1: Schematic diagram of LiF-TEA RICH system.

The photosensitive detector is really the starting point for the system design. We chose a multiwire proportional chamber filled with a mixture of Triethylamine (TEA) gas and Methane because it has good quantum efficiency (up to 35%) in a narrow wavelength interval between 135-165 nm, and an absorption length of only 1/2 mm. Other choices such as TMAE gas or phototubes would have taken most of our allotted 16 cm of radial space, and thus not allowed a full size detector to be constructed. Other solutions such as DIRC [2] were not feasible due to the existing detector iron and the desire to limit the detector thickness to less than 12% of a radiation length.

The position of Cherenkov photons is measured by sensing the induced charge on array of 7.6 mm x 8.0 mm pads. Since the pulse height distribution from single photons is exponential, this requires the use of low noise electronics. A dedicated VLSI chip, called VA_RICH, based on a very successful chip developed for solid state applications, has been designed and produced for our application at IDE AS, Norway. We have fully characterized hundreds of 64 channel chips, mounted on hybrid circuits. For moderate values of the input capacitance C_{in} the equivalent noise charge

measured ENC is found to be about:

$$ENC = 130e^- + (9e^-/pF) \times C_{in} \quad . \tag{1}$$

Its dynamic range is between 450,000 and 900,000 electrons, depending upon whether we choose a bias point for the output buffer suitable for signals of positive or negative polarity or we shift this bias point to have the maximum dynamic range for signals of a single polarity.

Two VA_RICH chips are mounted on a hybrid circuit. These are attached via miniature connectors to the back of the cathode board of the photon detectors. We group 5 hybrids (10 chips) into a single readout cell cabled to data boards located in VME crates just outside the detector cylinder. Chips in the same readout cell share the same control signals and bias lines from the data boards and output lines from the hybrid to the detector.

The analog output of the VA_RICH is transmitted to the data boards as a differential current, transformed into a voltage by transimpedance amplifiers and digitized by a 12 bit differential ADC. These receivers are part of complex data boards which perform several important analog and digital functions. Each board contains 15 digitization circuits and three analog power supply sections providing the voltages and currents to bias the chips, and calibration circuitry. The digital component of these boards contains a sparsification circuit, an event buffer, memory to store the pedestal values, and the interface to the VME cpu.

If a track is incident normal to a LiF radiator no light is emitted in the wavelength range that can be detected by TEA, due to total internal reflection. A full system for CLEO, therefore, would require that the radiators be tilted until the track angles are about 15°. This causes several serious problems. One is the difficulty in accurate radiator mounting. More importantly, some of the light from one radiator must traverse through another radiator resulting in lost light and reconstruction problems. To eliminate these problems a novel radiator geometry has been proposed [3]. It involves cutting the outer surface of the radiator with a profile resembling the teeth of a saw, and therefore it is referred to as a "sawtooth radiator" [3]. The major advantage of this configuration is that it reduces the losses of photons due to total internal reflection at the interface between the radiator and the expansion region. It also turns out that the angular resolution per photoelectron is greatly decreased [4].

A crystal profile with teeth about 4 mm deep in a plate of 12 mm thickness is a good compromise between uniformity in light output, and cost. A detailed simulation has shown that a tooth angle of 42° is close to optimal and technically feasible. Fig. 2 summarizes the results of this study, which focuses on particles with $p = 2.8$ GeV/c. The mean number of reconstructed photoelectrons, N_{pe}, Cherenkov angle resolution per photon, Cherenkov angle resolution per track, and the probability for a π to fake a K are plotted as a function of the angle θ between the charged particle and the normal to the radiator inner surface.

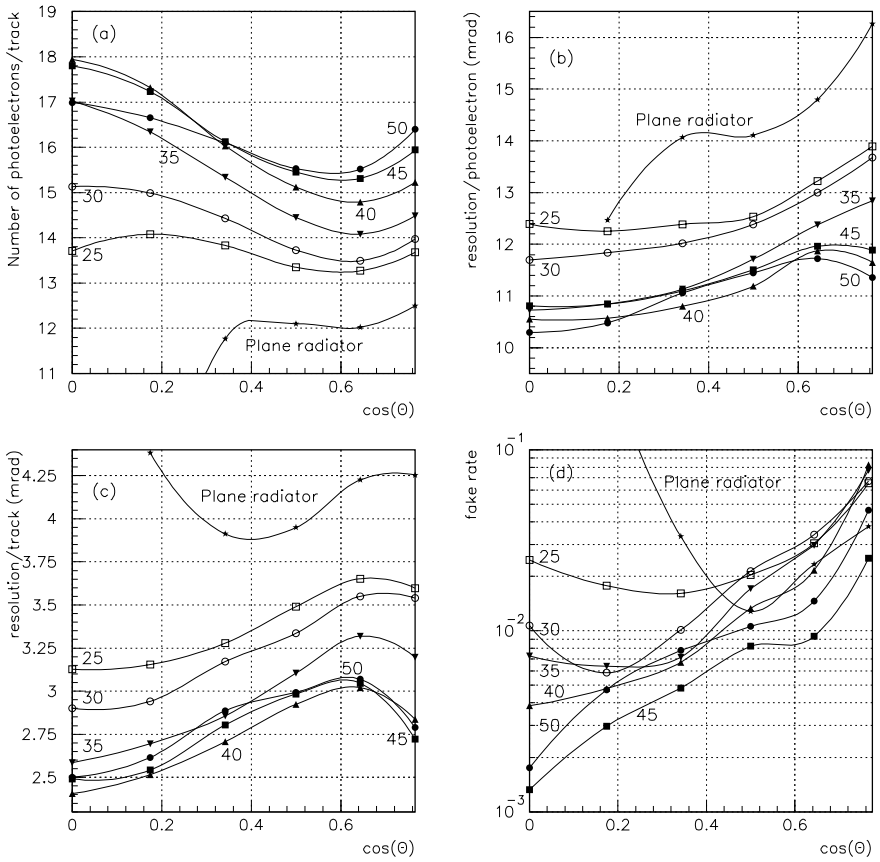

Figure 2: Performance of the sawtooth radiator as a function of the incident track angle. (Normal incidence is described by $\cos(\theta)$ of 0.) The curves are parametrized by the sawtooth angle: (a) The average number of detected photoelectrons, (b) The angular resolution per photon, (c) the angular resolution per track as a function of incident track angle, (d) the probability for a 2.8 GeV/c π to fake a K for 95% π detection efficiency.

The fake rates shown in Fig. 2(d) can be estimated accurately for the plane radiator by using the 12.8 mr Cherenkov angle separation coupled with the estimated resolution per track. However, such a procedure is far too optimistic in the case of the sawtooth radiator. The cause of the worsening of the fake rate is the that the image pattern of the photons is not described by a single curve as in the case of the plane radiator. In fact the image has two main branches and two secondary branches which contain <10% of the photons. The predicted image pattern for tracks normally incident on a sawtooth is shown in Fig. 3. The possibility for multiple interpretations of a photon path is responsible for the worsening of the fake rate. In the data analyzed here only the two main branches are considered.

There are several problems inherent in producing such radiators, including the ability to precisely cut the LiF without cleaving the material and the ability to polish the surface to yield good

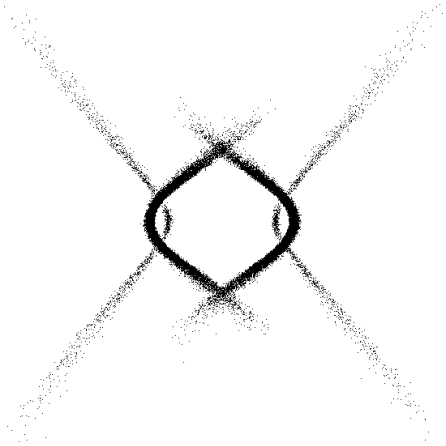

Figure 3: Cherenkov photon pattern on the detector plane for a track at normal incidence to a sawtooth radiator. The lense densely populated paths result from a combination of one refraction and one reflection.

ultraviolet light transmission. Furthermore, the production time and cost need to be reasonable. We worked with OPTOVAC in North Brookfield Mass. to produce two full sized radiators. A close up of two sawtooth radiators separated by a plane radiator is shown in Fig. 4.

Figure 4: Two sawtooth radiators separated by a plane radiator. The teeth are aligned perpendicular to one other in this test beam setup.

Transparency measurements for the two sawtooth radiators have been made relative to a plane polished sample of LiF. The transmissions for both pieces are very good. One exceeded the normally polished sample by 10% while the other was equal to it. The measurements for the better sample are shown in Fig. 5.

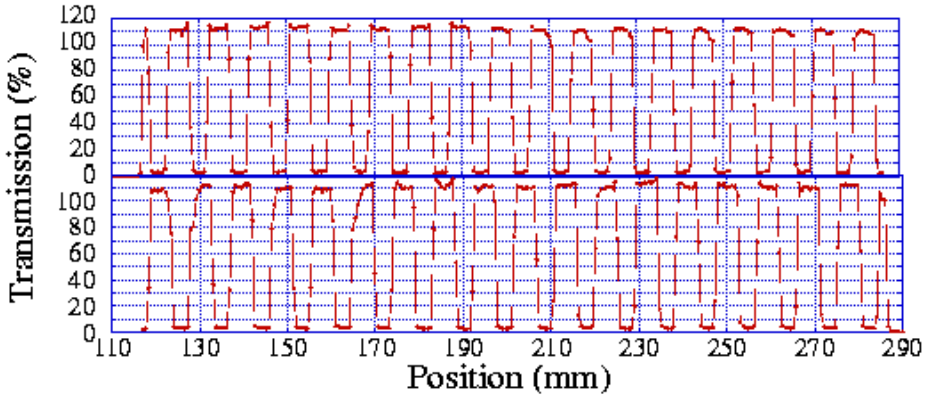

Figure 5: Optical transmission of prototype sawtooth radiator relative to a 45° prism polished with conventional techniques at 157 nm. The top curve is for the left side of the 19 teeth and the bottom curve is for the right side.

A sketch of a photon detector module is shown in Fig. 6. The MWPC anode wires run the

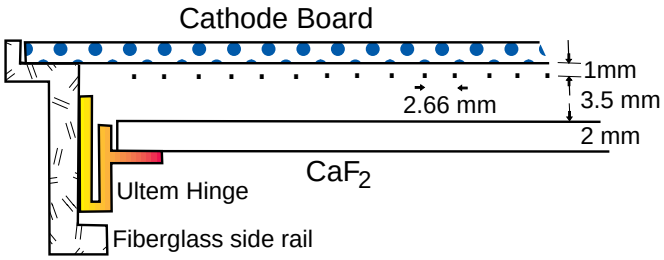

Figure 6: A cross-section of one RICH photon detection module.

entire length of the detector, approximately 2.5 m. They are supported every 30 cm by a ceramic spacer. The CaF_2 window joints are placed directly on top of these spacers to minimize the loss of photon acceptance.

A fully constructed module RICH photon detector module is shown in Fig. 7. It is mounted on a strongback, which is removed after assembly into the chamber holding structure. Construction of these chambers proceeded after successful prototype testing [5].

2 Test Beam Results

Two completed CLEO III RICH modules were taken to Fermilab and exposed to high energy muons (> 100 GeV/c) emerging from a beam dump. The modules were mounted in a leak tight aluminum box with exactly the same scheme as we will use in the final detector. Two sets of wire chambers were set up in the beam line to provide track direction and there were scintillators to provide a trigger. The data acquisition system was a prototype for the final CLEO system.

Figure 7: One of the 30 needed photon detector modules.

Beam conditions were much worse than expected. The particle flux was ten times higher than anticipated, due in large part to the experimenters in front of us lowering their magnetic field. In addition there was a large neutron background. We survived by receiving dedicated beam time at much lower intensity. Still the background conditions and particle fluxes are much higher than we expect in CLEO by about two orders of magnitude and we don't expect significant neutron background in CLEO.

For this test we read out every channel in every event. This proved to be quite useful because we found a rather large coherent noise component of about 1000 electrons whose source was imperfect grounding of the system and noisy switched power supplies in the DAQ crates. (These will be replaced in the final system.) However, we removed virtually all of the coherent noise by averaging the non-hit channels on each hybrid card and generating an event-by-event pedestal correction. We became so enamored of this procedure that we are adapting it in the final CLEO data boards. Thus our final noise value is approximately 400 e^- r.m.s. per channel. Furthermore, this trick will probably be used to lower noise in the CsI calorimeter system and will possibly be used for the silicon vertex detector.

The pulse-height distribution of candidate photon pad clusters after a 5σ cut above the noise is shown in Fig. 8(a). The distribution has been background subtracted. The pulse-heights follow an exponential distribution as expected. Fitting the slope provides a measurement of the gain; actually the fraction of the gain seen on the pad plane. We call this the pad gain. The pulse-height distribution for the charge tracks is much higher.

The number of observed photons as a function of pad gain, uncorrected for background, is shown in Fig. 8(b). Our operating point for these tests is a pad gain of about 40,000 and is on plateau.

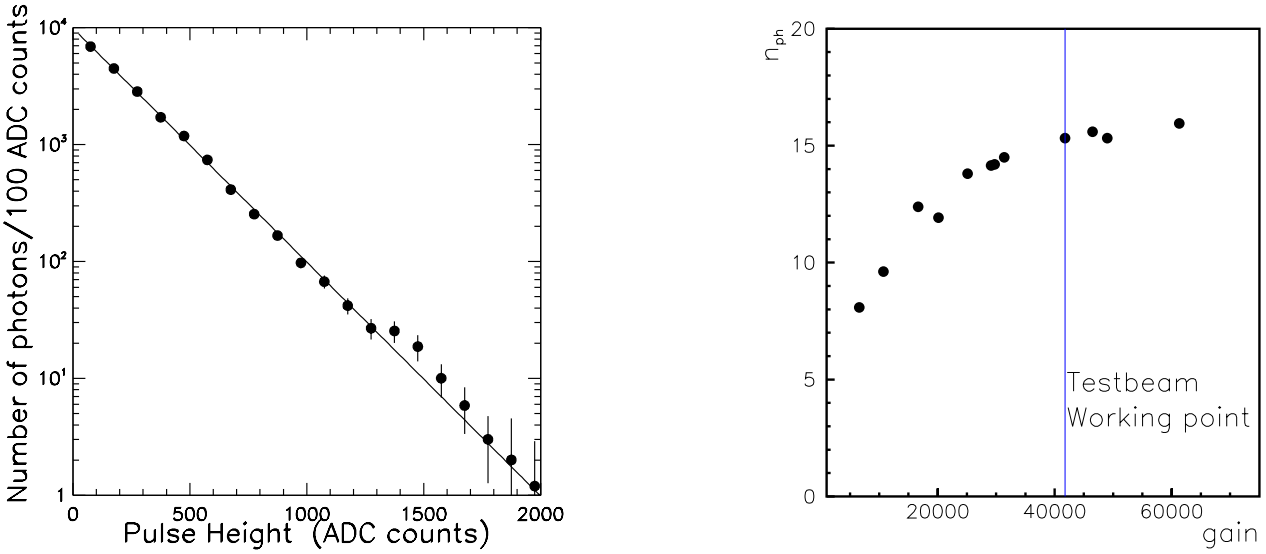

Figure 8: (a)The pulse height distribution for hits 5σ above noise from photon candidate clusters. (b) The number of observed photons, including background, as a function of pad gain.

For the plane radiator, we were able to configure the detector so that the photon pattern would appear only in one chamber. For the sawtooth radiator we would have needed three chambers to fully contain the image. Sample images from the plane and sawtooth radiators are shown in Fig. 9. Here the track was incident at 30° to the plane radiator and zero degrees for the sawtooth.

The best way to ascertain the expected performance is to first view the number of photons and the angular resolution per photon. In Fig. 10(left) we show the Cherenkov angle for all photons from many tracks. Fitting to a Gaussian with an asymmetric tail and quadratic background gives an angular resolution per photon of about 13.5±0.2 mr and a background of 8.8%. The asymmetric tail is due to the chromatic error [7].

Our Monte Carlo simulation includes information on CH_4-TEA quantum efficiency as a function of wavelength, crystal transmissions, etc... The background under the single photon peak has been modeled and included in our simulation. We think the background is mostly due to out of time tracks and that the background level in CLEO will be much smaller. The Monte Carlo simulation is in good agreement with the angular resolution per photon, and, after being adjusted to yield more photons, is also in good agreement with the photon distribution. From these data we can estimate the expected resolution per track, and compare to what we measure. The results presented here are preliminary; we have more data to analyze and the reconstruction algorithms are undergoing improvement.

Fig. 10(right) shows the number of detected photons per track, before background subtraction. The average number, after background subtraction, is approximately 14. Including some smearing from the background, we estimate the final average resolution per track to be 3.9 mr. However,

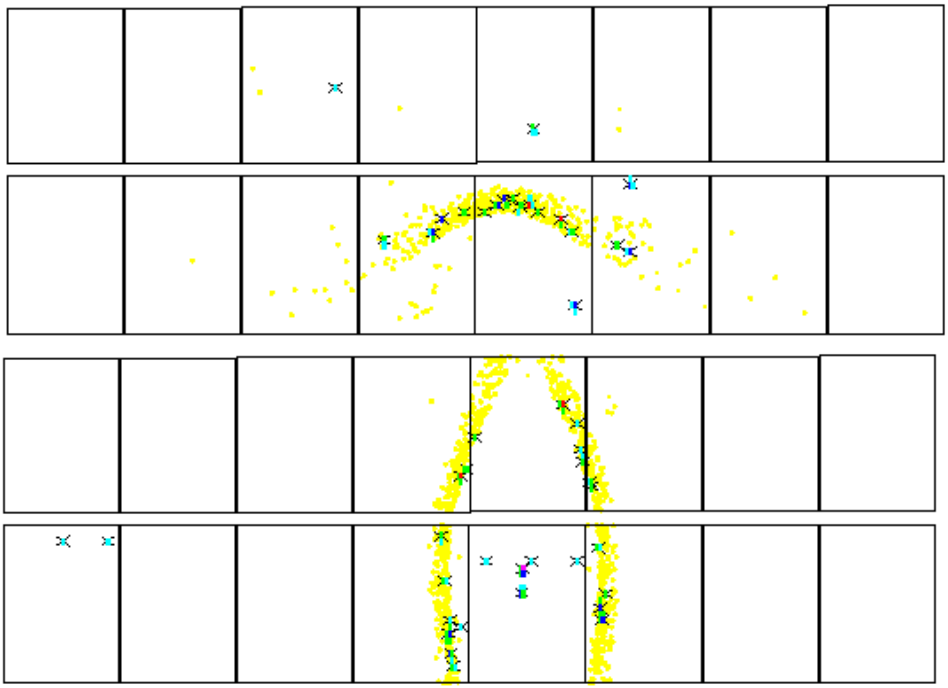

Figure 9: Single event images from the plane (top) and sawtooth (bottom) radiators. The light yellow points are where photons are expected to hit the detector plane. The green and blue points are photon hits and the crosses mark the reconstructed photon positions. The red point between the two arcs of the lower images shows the charged track impact point.

we have not included any error from the tracking system. Monte Carlo simulation of our tracking system shows that it contributes a 2.3 mr r.m.s. error [6]. Thus we expect a resolution of 4.5 mr on the Cherenkov angle per track, which is what we observe in Fig. 11. Most of the tracking error contribution comes from inaccurate prediction of the impact point of the track on the radiator, rather than a poorly determined track angle. We expect this to be substantially better in CLEO III, and thus expect to achieve our goal of 4.2 mr resolution. The pion momentum distribution from $B^o \to \pi^+\pi^-$ is a box shaped spectrum from 2.5 to 2.8 GeV/c, spread by the Doppler shift due to the B momentum. The angular separation between K and π at 2.8 GeV/c is 12.8 mr. Thus 4.2 mr resolution will provide better than 3σ K/π separation for all B decays [8].

In Fig. 12 and Fig. 13 we show similar plots for the sawtooth radiator. We see the expected improvement in angular resolution per photon of 11.8±0.2 mr. Here the Monte Carlo predicts a slightly better resolution. The number of observed photons is approximately 13.5. The measured Cherenkov angular resolution per track is 4.8±0.05 mr. The Monte Carlo prediction is 4.1 mr. We are not sure of the sources of this disagreement but it is possible that the crystal alignment is not adequate or that we do not know the sawtooth angle precisely enough. The number of photons needs to be corrected upwards by a factor of 1.7 since we do not have complete acceptance for

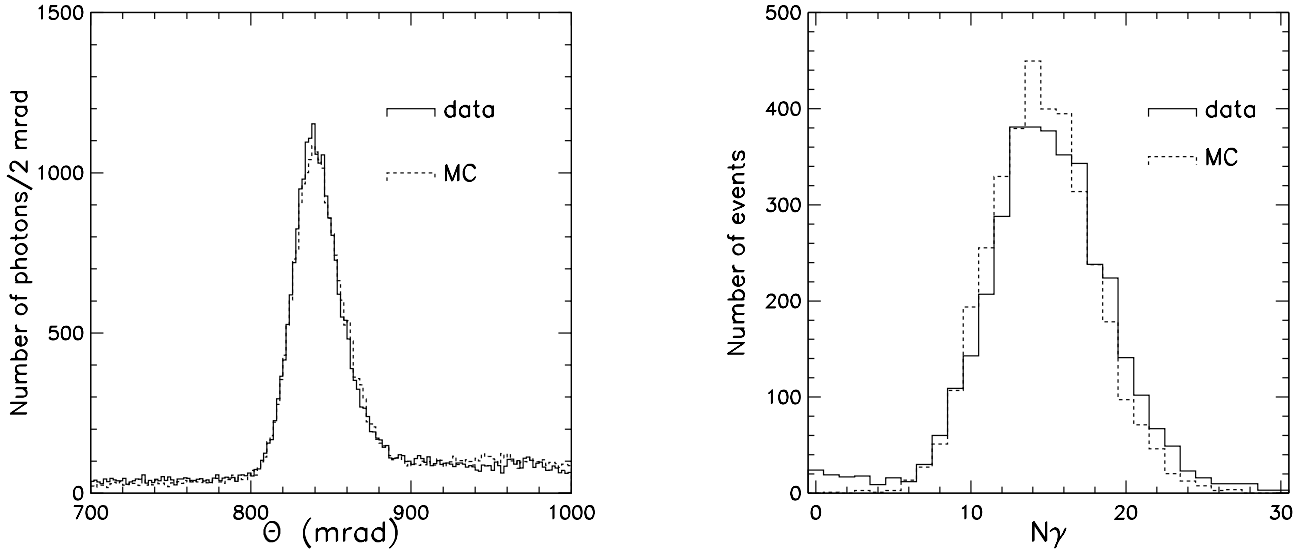

Figure 10: Results from test beam studies compared with Monte Carlo simulation for a plane radiator with tracks at 30° incidence. (left) The Cherenkov angle of each photon for a sum over many tracks. (right) The number of photons for each track.

both branches of the sawtooth image. For full acceptance we calculate 20 photons on average, after removing the 9% background. The sawtooth radiators work and we will use them for 3/7 of the detector, which covers 5/8 of the available solid angle.

3 Conclusions

Fig. 14 shows the measured resolution per track for the plane and sawtooth radiators as a function of the background subtracted number of photons detected. The curves are fits to the parameterization $(a/\sqrt{n})^2 + b^2$. Unfortunately, the parameters a and b have no relevant meaning since their errors are completely anti-correlated.

Table 1 summaries the achieved and predicted track resolutions.

Table 1: Track resolutions (mr)

Radiator	Data	Monte Carlo†	MC no background & no tracking errors	CLEO expectations
plane (30°)	4.5±0.07	4.5	3.9	4.0
sawtooth (0°)	4.8±0.05	4.1	3.8	2.9-3.8

† Statistical errors on the Monte Carlo samples are ±0.04 mr.

These data though preliminary show that we have a good understanding of the system and

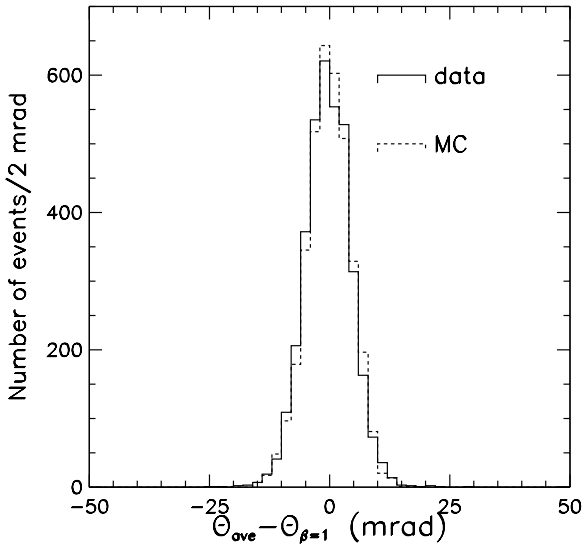

Figure 11: The Cherenkov angular resolution per track for a plane radiator with tracks at 30° incidence.

we can expect the predicted levels of efficiency versus rejection in CLEO III. Furthermore, the chambers held voltage, the electronics functioned, and the gas system worked, in much more difficult environment than will be present in CLEO. We have data for several additional incident angles for both plane and sawtooth radiators. After we have analyzed these data and understood the systematic errors in more detail, we will present more complete results in a later publication.

4 Acknowledgments

We thank Fermilab for their cooperation in providing a high energy particle beam and computing. Especially noteworthy for their help were Chuck Brown and Joel Butler. Franz Muheim and Stephen Playfer played major roles in the early stages of this work. Jacques Seguinot and Tom Ypsilantis provided initial insights and encouragement. We appreciate the help of our CLEO colleagues, especially Chris Bebek, Jeff Cherwinka, Charlie Strohman and Frank Wurthwein. Support was provided by the National Science Foundation and the Department of Energy.

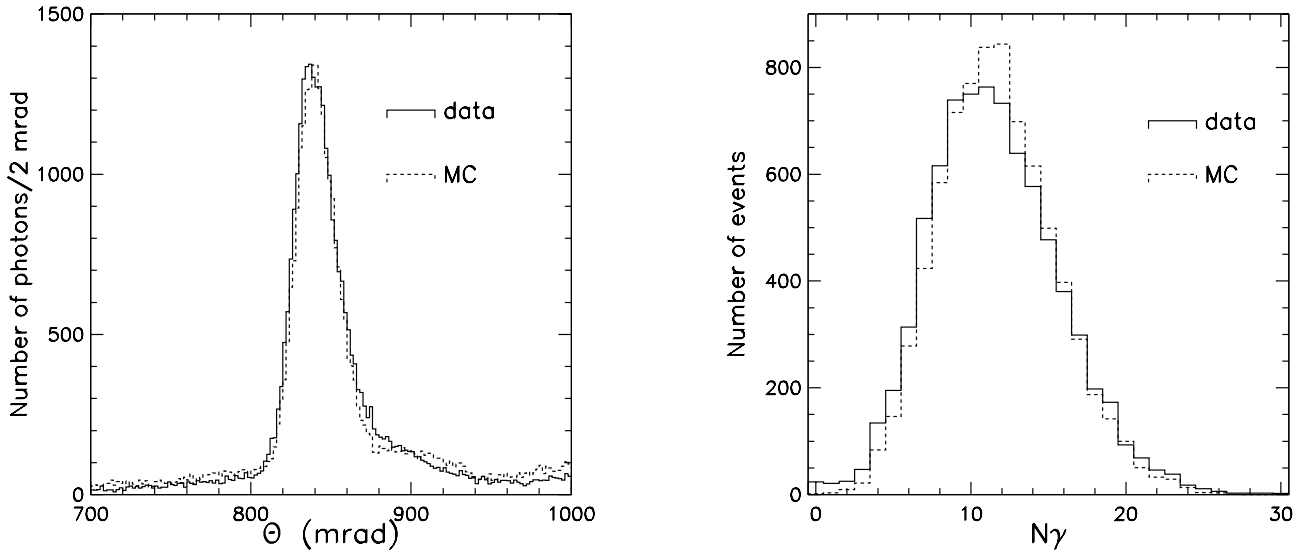

Figure 12: Results from test beam studies compared with Monte Carlo simulation for a sawtooth radiator with tracks at normal incidence. (left) The Cherenkov angle of each photon for a sum over many tracks. (right) The number of photons for each track.

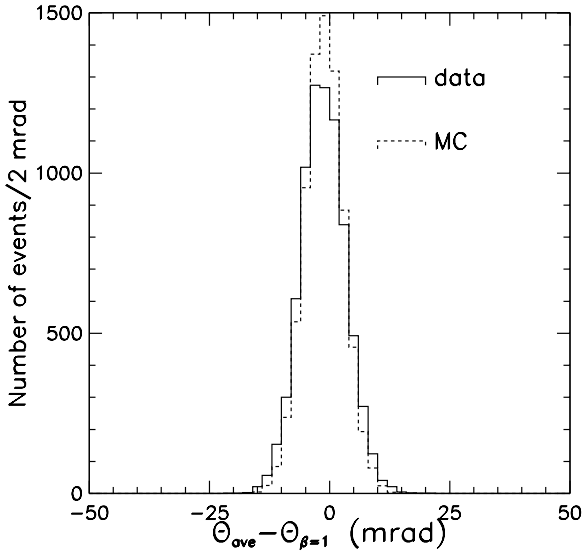

Figure 13: The Cherenkov angular resolution per track for a sawtooth radiator with tracks at normal incidence.

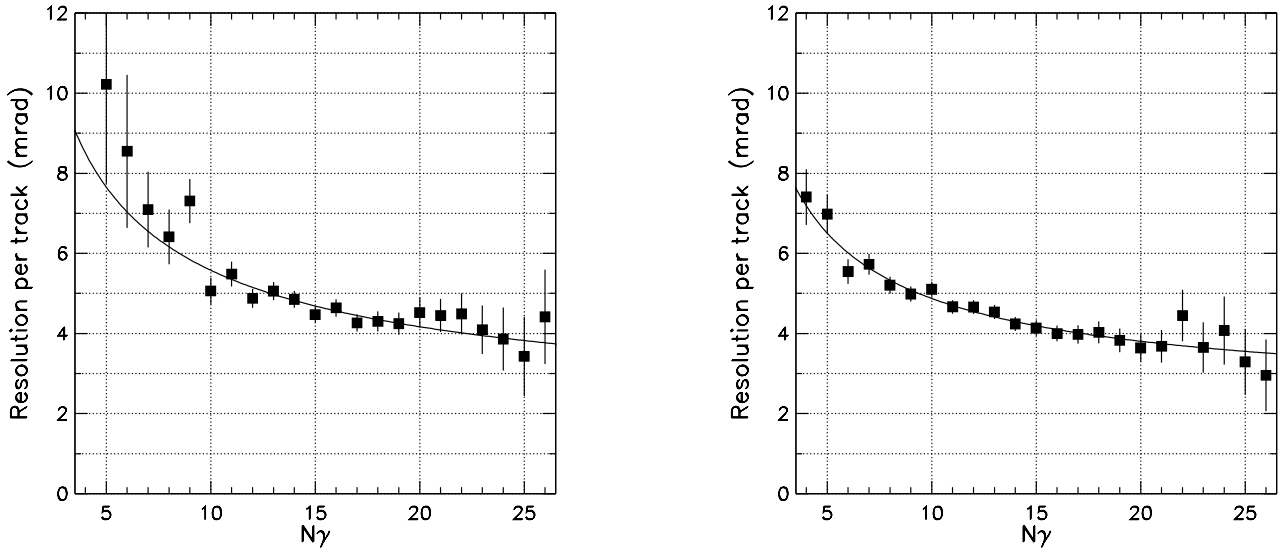

Figure 14: The Cherenkov angular resolution per track as a function of the number of detected photons (background subtracted) for a plane radiator with tracks at 30° incidence (left) and for a sawtooth radiator with tracks at normal incidence (right).

References

[1] R. Arnold *el al.*, *Nucl. Inst. and Meth.* **A314** (1992) 465.

[2] B. Ratcliff, *Nucl. Instr. and Meth.* **A343** 292 (1994).

[3] A. Efimov *et al.*, *Nucl. Instr. and Meth.* **A365** 285 (1995).

[4] The improvement in angular resolution per photon is due to the reduced refraction at the LiF-N_2 interface. Thus the angular spread due to chromatic dispersion is not magnified as much for the sawtooth radiator as it is for the plane radiator.

[5] S. Playfer *et al*, *Nucl. Instr. and Meth.* **A371** 321 (1996).

[6] We used 30 cm^2 wire chambers borrowed from Fermilab which had 5 mm wide cells. We equipped the wire readout with TDC's, also borrowed from Fermilab, but have not implemented the TDC readout. If time permits we can, in principle, improve the tracking errors.

[7] We have not quoted systematic errors on the various measured resolutions in this paper. The systematic errors are likely to be as large if not larger than the statistical errors, and thus we emphasize the preliminary nature of these results.

[8] We also expect to have 2σ π/K separation at 2.8 GeV/c from the dE/dx system in the drift chamber.

ELECTRON MULTIPLICATION AND SECONDARY SCINTILLATION IN LIQUID XENON: NEW PROSPECTS

A.J.P.L.Policarpo, V.Chepel, M.I.Lopes and R.Ferreira Marques
LIP-Coimbra and Physics Department of the University of Coimbra
University of Coimbra, 3000 Coimbra, Portugal

ABSTRACT

The history, present situation and prospects on electron multiplication and secondary scintillation in liquid xenon and their application to radiation detectors are shortly discussed.

1 Introduction

Proportional charge multiplication and secondary scintillation are two effects of great importance for radiation detection. Intrinsic amplification in a detector, which becomes possible thanks to these mechanisms, notably improves the detector performance. Apart from reducing requirements to the front end electronics, the intrinsic amplification results in significant increase of signal-to-noise ratio and, as a consequence, allows the detection of particles that deposit in the detector very low energy with good energy resolution. Moreover, the influence of positive ions, produced by an ionizing particle along its track, on the signal amplitude can be neglected. The essence of proportional multiplication is that electrons, drifting in a strong electric field, gain enough energy to ionize the atoms and/or molecules of the medium. Overall, every primary electron can produce thousands of secondary electrons. Thus, yielding a total collected charge at the detector output proportional to the ionization charge (energy deposit) produced by the incoming particle.

Typically, the practical electric field threshold for achieving charge multiplication in gas is E/p^a~5 to 10 V/cm/Torr (E/N >1.4x10^{-16} Vcm^2), where E is the electric field strength, N the number of atoms/molecules of the gas per cubic centimeter and p the pressure.

Secondary scintillation does not require such a high field as charge multiplication of the charge as the drifting electrons do not ionize the gas but just excite its atoms. The threshold field for secondary scintillation in noble gases is about E/p~1 V/cm/Torr (E/N~3x10^{-17} Vcm^2). The scintillation light, mostly UV or VUV, emitted is commonly detected by photomultiplier tubes. One drifting electron can produce up to hundreds of

photons reaching the photomultiplier, resulting in tens to hundreds of photoelectrons emitted from the photocathode. Employing the secondary scintillation allows very good energy resolution to be achieved as the statistics of charge multiplication is avoided.

In general, excitation of the gas by drifting electrons always precedes charge multiplication. In proportional counters, however, the light emission plays a negative role. It may give rise to electric discharges due to possible photoelectric emission of electrons at the cathode thus resulting in positive feedback in the chamber. Therefore, quenching admixtures are usually added to the main detecting gas, in order to suppress the light emission or shorten its mean free path, thus allowing to achieve higher charge gains. For example, in gaseous xenon, which is the most efficient g-ray absorber, an order of magnitude higher gain can be achieved with Xe/CH_4 mixture than with pure xenon [1]. Conversely, employing secondary scintillation requires the gas to be pure. It is very important to keep in mind this point when one considers the possibility of electron multiplication or secondary scintillation in liquid xenon as the purity requirements in the liquid are much more severe than in the gas. Concentration of electronegative impurities of ~10 ppb (oxygen equivalent) limits the electron life time to a few ms and is not acceptable for many applications.

Liquid xenon detectors were recently proposed for various applications: as electromagnetic calorimeters for high energy physics [2,3], for gamma ray detection in astronomy [4], as a time projection chamber for particle physics experiments [5], imaging detectors for nuclear medicine [6,7]. These detectors work either in ionization or in primary scintillation mode or combine both of them, i.e. with no intrinsic amplification in the chamber. However, even a moderate charge amplification is highly desirable. This justifies the efforts that were and are being made in order to study the possibility of achieving both multiplication and secondary scintillation in liquid xenon detectors, which is the subject we shall discuss below.

2 Historical survey

The first observations of the electron multiplication in condensed noble gases were reported 50 years ago by Hutchinson [8]. Twenty years later, in the beginning of the 70s, a detail investigation of multiplication in liquid xenon in view of possible applications for radiation detection was initiated by L.W.Alvarez and carried out independently in several laboratories [9-12]. The ultimate goal of replacing the gas in the proportional chamber with a liquefied noble gas was to improve the position resolution. Indeed, increasing the density of the detecting medium would result in an increase of the number of ion pairs produced by a minimum ionizing particle within the detector, thus allowing a more accurate definition of

the center of gravity of the electron distribution and, therefore, better localization. In addition, this is accompanied by the suppression of electron diffusion and delta-ray range. Furthermore, the decrease of the detector thickness decreases the localization uncertainty due to parallax. Alternatively, sacrificing spatial resolution, a thick chamber can be produced providing high detection efficiency of g-rays.

A maximum gain of about 200 has been obtained in a liquid xenon single wire cylindrical proportional chamber with very thin anode wires using as a radioactive source either an internal ^{207}Bi, which emits conversion electrons and g-rays of energy of about 0.5 MeV and 1 MeV, or an external g-ray source ^{137}Cs (662 keV) or ^{207}Hg (85 keV and 279 keV). It was found that multiplication in the liquid occurs at E/N significantly lower than one could expect from a simple extrapolation of the data obtained in gaseous xenon to the liquid densities. Nevertheless, wires of 3 to 5 mm diameter are required to obtain electric field strengths of ~1 MV/cm near the anode surface at the applied voltage of several kV. An energy resolution of about 22%, fwhm, was measured for 279 keV g-rays with the 3.5 mm wire at gain of 10 [10]. The resolution becomes worse at higher gains. A poor energy resolution roots, apparently, in the non-uniformity of the wire diameter and probable irregularities on its surface (one can roughly estimate that variations of the diameter of 1% can cause differences in the gain of ~30%).

Chambers of 6 to 10 mm cathode diameter were experimented by different authors [9-12]. A saturation of the charge pulse amplitude after reaching a gain of ~200 due to accumulation of positive space charge near the wire was observed. For example, a reduction of the count rate from 2000 to 200 s^{-1} resulted in an increase of the saturation amplitude by a factor of 3 [10] (for the cathode diameter of 8 mm), showing that the low mobility of positive ions in liquid xenon constitutes a real problem for the practical use of the electron multiplication.

The first Townsend coefficient, a, was computed by fitting the experimental data with 9 adjusting parameters [10]. It was found to be 27 times larger than it would be in gaseous xenon with the same density showing that liquid xenon is not just a compressed gas. The maximum reported value of $a=(4.47\pm0.26)\times10^4$ cm^{-1} was obtained at E=2 MV/cm. The results were, however, questioned by T.Doke, since the fit does not converge to the right W-value and recombination constant [13]. The coefficient a was also derived by Prunier et al. [11] from independent measurements. The values reported were close to those obtained by Derenzo et al. at fields above ~0.8 MV/cm, but the W-value suffers from the same inconsistency with other data.

An attempt to build a multiwire proportional chamber has been undertaken [14]. However, much higher voltages were required to reach the same gain as in a single wire counter and, practically, it was difficult to operate the chamber at a gain higher than 10.

Such thin wires are very difficult to handle; they can be easily damaged by electrical discharges. In addition, the electrostatic repulsion between the wires in a multiwire chamber is so strong that frequently leads to breaking the wires, just due to application of a high voltage, and special means (wires interlaced with quartz fibers) were necessary to keep the wires in a plane. Thus, although the first results were very promising and significant and reproducible multiplication of electrons in liquid xenon has been obtained, the technical difficulties associated to practical applications are such that this line of research was practically abandoned.

Secondary scintillation of liquid xenon has been first observed by Dolgoshein et al. [15] in a uniform electric field. The threshold field was found to be ~100 kV/cm. Later, it was studied by a Japanese group [16, 17] in a cylindrical geometry with wires of 4 to 20 mm diameter. Although, the authors do not present the absolute number of photons emitted, one can roughly estimate it to be ~10 to ~100 photons per primary electron, depending on the applied voltage, for the 4 mm anode wire. The lowest value corresponds to a voltage at which there is essentially no charge multiplication while the highest one was obtained for a charge gain of ~50 was observed.

Assuming the same linear relationship between the number of photons per electron and the electric field strength, found for gas, the authors made a fit to the measured data and found the threshold field for secondary scintillation in liquid xenon to be surprisingly high. A value ranging from 400 kV/cm to 700 kV/cm was derived, which is much larger than the one previously obtained [15] and very close to the field at which the electron multiplication occurs. However, these figures are consistent with the value calculated considering liquid xenon as compressed gas at 520 bar.

Proportional scintillation could also be observed with thicker wires. With the wire of 20 mm diameter, ~5 photons per electron are emitted at an anode voltage of 5 kV, as estimated by T.Doke [18] (our estimate, using the same method as above and taking into account the scintillation light yield for liquid xenon measured in [19], gives the value of ~20 photons per primary electron). For a 50 mm wire, the figure of ª30 photons per electron was estimated to be achievable at the anode voltage of 12 kV [20].

However, the energy resolution as good as expected has not been obtained. It was measured to be about 16-20% for 1 MeV electrons, almost independently of the wire diameter [16]. The same 16% resolution was also obtained when the chamber was operated in ionization mode. The authors attribute this fact to imperfect charge collection onto the

wire in that particular chamber geometry. In a better geometry, the resolution of 15% was measured for alpha-particles [17]. In order to compare this value to that obtained with electrons, one should take into account that due to high ionization density along the alpha-particle track in liquid xenon, only a few percent of the electrons escape the recombination in the field of ~10 kV/cm. Thus, the number of electrons collected onto the anode wire in this experiment corresponds to an energy deposition of ~250 keV by a minimum ionizing particle. To our knowledge, there are no other experimental results published in the literature showing that a better energy resolution has be achieved.

Secondary scintillation was used in a liquid xenon drift chamber built for precise localization of charged particles (20 mm, r.m.s.) [17] or annihilation g-rays (0.9 mm, fwhm) [21]. Recently, a liquid xenon detector was developed for detection of WIMP's (Weak Interacting Massive Particles) [22]. Detection of the xenon primary and secondary scintillation from the same event allows to discriminate the background, mainly due to minimum ionizing particles, and to detect the recoil nuclei with high signal-to-noise ratio. Secondary scintillation, with an increase in the photon yield relatively to the primary scintillation by a factor of 10 (for 122 keV g-rays; 4.5 mm wire), was measured and the information obtained allowed the design of a prototype of a 700 cm^3 chamber. To our knowledge, this is the first reasonably sized device designed with the specific aim of using intrinsic gains with liquid xenon, towards a well defined physics experiment.

3 Charge multiplication with new microstructures

The development of new microstructures, such as microstrip and microgap chambers, refreshed the interest for electron multiplication in liquid xenon. Indeed, not only such devices can be made with anode strips of several micrometers width and thus substitute thin fragile wires, but also the short anode to cathode distance allows the fast collection of positive ions. It is interesting to note that the advantage of such a kind of device was recognized more than 20 years ago: the "development of a practical high-resolution chamber of large size requires replacement of the stretched fine wires by conductive strips laid down on an insulating substrate" [9].

The electron multiplication in a microstrip plate (MS) has been observed in liquid xenon by us and is reported in the literature [23]. A plate of ILL-6C type was used for the measurements. It has anode strips of 8 mm width, cathodes of 400 mm width and 1000 mm anode pitch. The strips, made of nickel, are deposited on Desag D236 glass (Fig.1). An ^{241}Am alpha-source of 4 mm diameter was deposited on the drift electrode 1.9 mm away from the MS plate surface and parallel to it. All the anode strips were connected together, as well as all the cathodes. The negative voltage was applied to the drift electrode; cathodes were kept at the ground potential and a positive voltage applied to the anodes. Three signals were read from the chamber with low-noise charge-sensitive preamplifiers: at the anode strips, at the cathodes and at the drift electrode. The latter allowed to account for the recombination along the alpha-particle track which is a function of the drift field strength.

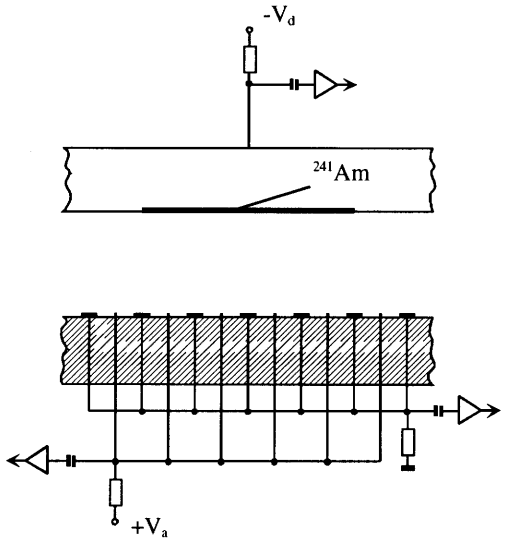

Fig.1 Schematic drawing of the liquid xenon chamber with a microstrip plate

The chamber was filled with carefully purified liquid xenon and cooled down to the temperature of about -60ºC being immersed into an ethanol bath cooled with liquid nitrogen.

With an increase of the anode voltage above 600 V (at constant drift voltage), the amplitude of the anode signals, normalized to those taken at the drift electrode (i.e., corrected for the charge yield from the particle track), started to rise while the signals at the cathode strips changes the polarity (Fig.2). The amplitude of the signals was determined as the position of the corresponding peak on the amplitude spectrum.

The interpretation of this plot is as follows. As the alpha-particle range in liquid xenon is of the order of tens of microns and the drifting electron cloud is broadened due to diffusion by ~100 mm, i.e. comparable with the distance between the cathode edge and the anode, and the source diameter is larger than the MS plate pitch, two possibilities may arise at low fields. First, the electrons extracted from each track can be collected almost totally either to the cathodes or to the anode strips, thus inducing negative charge signals with the amplitude equal to 1 (inverted in Fig.2) on the corresponding electrode. Second, the drifting charge can be split between the electrodes and this is the case for the anode potential <200 V at which the amplitude of the anode signal varies with the applied

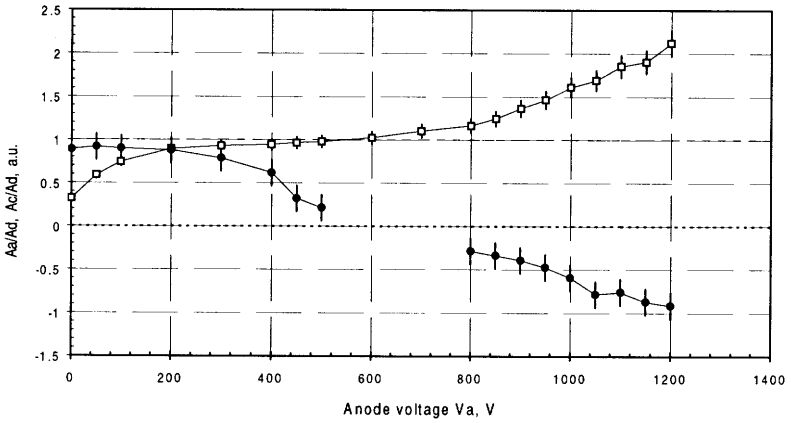

Fig.2 Anode and cathode signal amplitudes as a function of anode voltage [23].

Published with permission

voltage. An increase of the anode potential to 500 V results in complete charge collection to the anodes; the count rate at the anodes also increases at the cost of that observed at the cathodes; when the drifting charge is split, most of it is collected onto the anode strips, also yielding a decrease of the amplitude of the cathode signals. Up to this voltage, the results are fully explainable on the basis of collection conditions of the drifting electrons.

As one increases the anode voltage above 600 V, the electron multiplication starts. We observe both an exponential rise of the anode amplitude and the appearance of inverted pulses on the cathodes, induced by positive ions created near the anode surface and drifting towards the cathodes. The inequality of the amplitudes of the signals observed at the anodes and cathodes is, apparently, due to the long ion drift time estimated to be ~100 ms for the distance of 300 mm. Such long signals could not be measured correctly with our electronics. At the intermediate anode voltages, between 500 and 800 V, the signals of both polarities at the cathode strips could be observed with an oscilloscope, some of them

related with the collection of the electrons from the particle track to the cathodes while others being induced by those collected to the anode where the multiplication occurred.

At higher drift voltage, higher maximum multiplication gain could be achieved. At -2600 V applied to the drift electrode, we measured the gain of about 10 at the anode voltage of 1700 V. It was the highest voltage that we could apply to the anode. Further voltage increase resulted in unstable behavior and discharges.

The collection time of the positive ions in the MS chamber filled with liquid xenon is still long. It can be eventually reduced several times by using a plate with smaller distance between the anode and cathode strips. A more radical solution is to use a microgap chamber (MGC) instead. In this chamber, the anode strips are separated from the cathode plane by a thin insulating layer so that the drift path of the ions can be made of a few microns. In addition, a higher field strength at the anode surface is expected to be achieved at lower anode voltage. Therefore, we also experimented an MGC chamber produced in Delft Technical University [24] in liquid xenon. The experimental set-up and working conditions were essentially the same as for the MS chamber. However, discharges at anode voltage as low as 450 V did not allow to achieve the field strength at which the electron multiplication might possibly occur.

The MS plates and MGC chambers, in general advantageous when compared to wire chambers, have however one drawback: the existence of a dielectric surface supporting the electrodes significantly limits the operating voltage as it favors the occurrence of surface discharges. One could think about producing a substrate with a special profile in order to reduce the tangential component of the electric field at the dielectric surface (the leak microstructure [25] is an example) but it complicates the design and such a device can become too “bulky” for some applications (this is the case of the liquid xenon detector for PET, for instance [7], where the dead volume in the chamber has to be minimized).

A new microstructure, the so called “virtual cathode chamber”, which has recently been suggested for gas filled proportional detectors [26], may be an interesting option for a liquid xenon detector, as well. It attracts by the simplicity of the design and by having a bulk insulator (substrate) between the anode strips and the cathode layer deposited on the opposite side of the substrate (Fig.3) thus avoiding discharges.

In order to assess the possibility of charge multiplication with this device, we performed calculations of the electric field and the multiplication gain for the chamber shown in fig.3 and for various sets of potentials at the drift electrode and the cathode plane, assuming the anode strips to be kept at the ground potential. The field configuration obtained for V_d= -2000 V and V_c= -1800 V is shown in Fig.4. The calculations show that the field strength of >1 MV/cm, necessary for multiplication in liquid xenon, can be

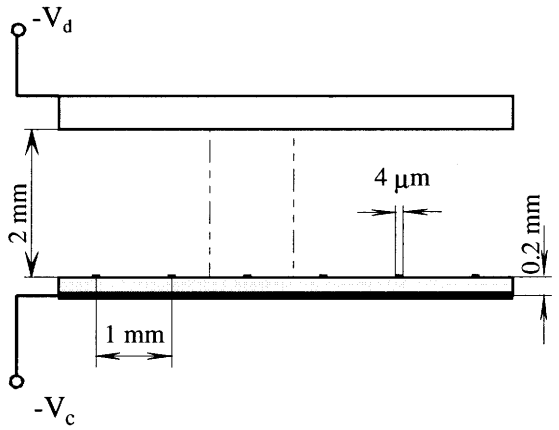

Fig.3 Virtual cathode chamber configuration considered in calculations. Selected central area corresponds to that shown in Fig.4.

achieved along a few mm close to the surface of the anode strip. Moreover, near the anode, the field varies with the distance much slower than ~1/*r*, typical of cylindrical geometry, thus being more favorable for the multiplication. We have found that the multiplication region of several micrometers is expected to result into a total gain of ~100 or higher. However, one should remember that since the multiplication is an exponential process, a small uncertainty in the first Townsend coefficient, which we took from [10], may lead to a significant error in the calculated gain. Nevertheless, even being pessimistic we believe that the considered microstructure has good prospects in what concerns both charge multiplication and secondary scintillation.

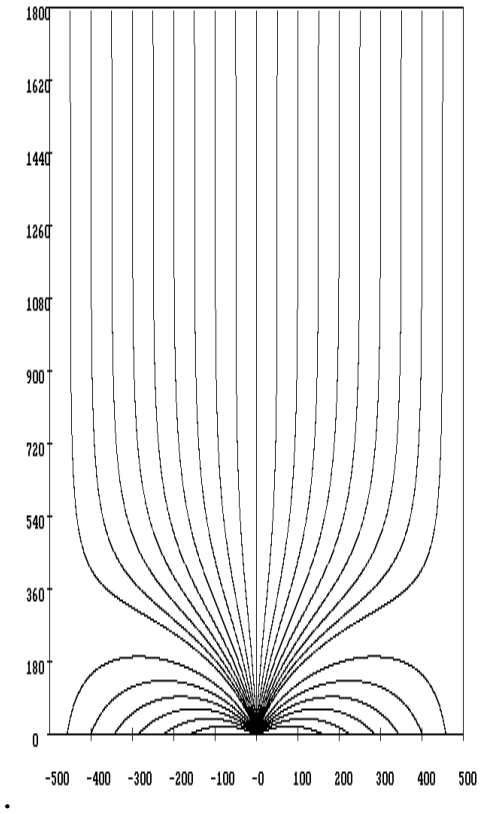

Fig.4 Field configuration in the drift region of the virtual cathode chamber shown in fig.3 with V_d= -1800 V and - V_d= -2000 V. Dimensions shown in the figure are in mm.

4 Conclusion

The possibility of taking profit from electron multiplication and secondary scintillation in liquid xenon radiation detectors, that were observed over 20 years ago and, at that time, did not find any practical applications due to technical difficulties, should be reconsidered, in view of the recent development of new reliable and easy to handle microstructures. The existing data, however, are contradictory and, therefore, additional studies of the multiplication and secondary scintillation processes are required.

References

[1] H.Sakurai and B.D.Ramsey. Dependence of Energy Resolution on Anode Diameter in Xenon Proportional Counters, *Nucl.Instr. and Meth. in Phys. Res.*, vol.A313, pp.155-160, 1992.

[2] J.Séguinot, G.Passardi, J.Tischhauser and T.Ypsilantis, Liquid Xenon Ionization and Scintillation. Studies for a Totally Active-Vector Electromagnetic Calorimeter, *Nucl. Instr. and Meth. in Phys. Res.*, vol.A323, pp.583-600, 1992.

[3] M.Chen, M.Mullins, D.Pelly et al. Homogeneous Scintillating LKr/LXe Calorimeters, *Nucl. Instr. and Meth. in Phys. Res.,* vol.A327, pp.187-192, 1993.

[4] E.Aprile and M.Suzuki, Development of Liquid Xenon Detectors for Gamma Ray Astronomy, *IEEE Trans. on Nucl. Sci.,* vol.NS-36, pp.311-315, 1989.

[5] G. Carugno, G.Pete, S.Cerdonio et al. Test of a Self Triggered Liquid Xenon TPC, Proc. Int. Conf. on Liquid Radiation Detectors, Waseda University, Tokyo, 1992, Ed. T.Doke, pp.104-108.

[6]V.V.Egorov,V.P.Miroshnichenko, B.U.Rodionov, A.I.Bolozdynya, S.D.Kalashnikov and V.L.Krivoshein. Electroluminescence Emission Gamma-Camera, *Nucl. Instr. and Meth.,* vol.205, pp.373-374, 1983.

[7] V.Yu.Chepel, M.I.Lopes, H.M.Araújo, M.A.Alves, R.Ferreira Marques and A.J.P.L.Policarpo. Liquid Xenon Multiwire Chamber for Positron Tomography, *Nucl. Instr. and Meth. in Phys. Res.,* vol.A367, pp.58-61, 1995.

[8] G.W.Hutchinson. Ionization in Liquid and Solid Argon, *Nature*, vol.162, pp.610-611, 1948.

[9] R.A.Muller, S.E.Derenzo, G.Smadja, D.B.Smith, R.G.Smits, H.Zaklad and L.W.Alvarez. Liquid-Filled Proportional Counter, *Phys. Rev. Lett.*, vol.27, pp.532-535, 1971.

[10] S.E.Derenzo, T.S.Mast, H.Zaklad and R.A.Muller. Electron Avalanche in Liquid Xenon, *Phys. Rev.*, vol.A9, pp.2582-2591, 1974.

[11] J.Prunier, R.Allemand, M.Laval and G.Thomas. Some Properties of Xenon Liquid-Filled Nuclear Detectors, *Nucl. Instr. and Meth.*, vol.109, pp.257-264, 1973.

[12] M.Miyajima, K.Masuda, A.Hitachi, T.Doke, T.Takahashi, S.Konno, T.Hamada, S.Kubota, A.Nakamoto and E.Shibamura. Proportional Counter Filled With Highly Purified Liquid Xenon, *Nucl.Instr. and Meth.,* vol.134, pp.403-405, 1976.

[13] T.Doke. Fundamental Properties of Liquid Argon, Krypton and Xenon as Radiation Detector Media, *Portug. Phys.*, vol.12, pp.9-48, 1981.

[14] H.Zaklad, S.E.Derenzo, R.A.Muller and R.G.Smits. Initial Images From a 24-Wire Liquid Xenon g-Camera, *IEEE Trans. Nucl. Sci.*, vol.NS-20, pp.429-431, 1973

[15] B.A.Dolgoshein, V.N.Lebedenko and B.U.Rodionov. Luminescence Induced by Alpha Particles in Liquid Xenon in an Electric Field, *JETP Lett.*, vol.6, p.224, 1967.

[16] K.Masuda, S.Takasu, T.Doke, T.Takahashi, A.Nakamoto, S.Kubota and E.Shibamura. A Liquid Xenon Proportional Scintillation Counter, *Nucl.Instr. and Meth.,* vol.160, pp.247-253, 1979.

[17] M.Miyajima, K.Masuda, Y.Hoshi, T.Doke, T.Takahashi, T.Hamada, S.Kubota, A.Nakamoto and E.Shibamura. A Self-Triggered Liquid Xenon Drift Chamber by the

Use of Proportional Ionisation or Proportional Scintillation, *Nucl.Instr. and Meth.*, vol.160, pp.239-246, 1979.

[18] T.Doke. Recent Developments of Liquid Xenon Detectors, *Nucl.Instr. and Meth.*, vol.196, pp.87-96, 1982

[19] M.Miyajima, S.Sasaki and E.Shibamura. Absolute Number of Photons Produced by Alpha-particles in Liquid and Gaseous Xenon, , *Nucl. Instr. and Meth. in Phys. Res.*, vol.B63, pp.297-308, 1992.

[20] A.J.P.L.Policarpo. Ionization Scintillation Detectors, *Nucl. Instr. and Meth.*, vol.196, pp.53-62, 1982.

[21] K.Masuda, T.Doke and T.Takahashi. A Liquid Xenon Position Sensitive Gamma-Ray Detector for Positron Annihilation Experiments, *Nucl.Instr. and Meth.*, vol.188, pp.629-638, 1981.

[22] P.Benetti, E.Calligarich, R.Dolfini et al., Detection of Energy Deposition down to the keV Region Using Liquid Xenon Scintillation, *Nucl. Instr. and Meth. in Phys. Res.*, vol.A327, pp.203-206, 1993.

[23] A.J.P.L.Policarpo, V.Chepel, M.I.Lopes et al. Observation of Electron Multiplication in Liquid Xenon with a Microstrip Plate, *Nucl. Instr. and Meth. in Phys. Res.*, vol.A365, pp.568-571, 1995.

[24] J. van der Marel, A. van den Bogaard, C.W.E. van Eijk, R.W.Hollander and P.M.Sarro. Two-Dimensional Microgap Gas Chambers on Silicon, *Nucl. Instr. and Meth. in Phys. Res.*, vol.A367, pp.181-184, 1995.

[25] M.Lombardi and F.S.Lombardi. The Leak Microstructure, Preliminary Results, *Nucl. Instr. and Meth. in Phys. Res.*, vol.A367, pp.23-27, 1995.

[26] M.Capeáns, W.Dominik, M.Hoch, L.Ropelewski, F.Sauli, L.Shekhtman, A.Sharma. The Virtual Cathode Camber, Preprint CERN-PPE/97-61.